Article:

Alqahtani, SA, Collier, REL orcid.org/0000-0002-8001-0510, Paton, DA et al. (2 more authors) (2022) Uplift evolution along the Red Sea continental rift margin from stream profile inverse modeling and drainage analysis. Journal of African Earth Sciences, 192. 104551. ISSN 1464-343X

https://doi.org/10.1016/j.jafrearsci.2022.104551

Uplift evolution along the Red Sea continental rift margin from stream profile inverse modeling and drainage analysis

S. A. Alqahtani[1], R. E. Ll. Collier[2], D. A. Paton[3] and G. G. Roberts[4], C. P. B. O'Malley[4]

[1]EXPEC Advanced Research Center, Saudi Aramco, Dhahran, Saudi Arabia

[2]School of Earth and Environment, University of Leeds, Leeds, UK

[3]TectonKnow Ltd, Settle, UK

[4]Department of Earth Science and Engineering, Imperial College London, London, UK

Corresponding author: Saleh Alqahtani (saleh.qahtani.20@aramco.com)

Abstract

Continental rifted margins can have complex uplift histories related to different processes including footwall uplift by mechanical unloading, dynamic uplift and interaction with transfer margins. Deciphering uplift histories along rift flanks is integral to understanding the margin evolution as a whole. Here, a combination of drainage analysis and stream profile inverse modeling is utilized to estimate the rift flank uplift along the north-eastern Red Sea onshore margin. The drainage network was extracted from an ASTER DEM (~30 x 30 m-horizontal resolution) and the uplift history was calculated using an inverse model, which builds on the relationship between uplift, erosion and stream profile shape. Local relief, minimum erosion volumes and minimum erosion volume:catchment area ratios (R_{va}) were also calculated and compared to uplift estimates. Within the study area, small catchments represent footwall drainage and larger catchments are mostly associated with pre-rift structures and syn-rift accommodation zones. Uplift initiated in the southern part during early rifting (21-15 Ma) before shifting northward (12-0 Ma). This uplift distribution is reflected in R_{va} and relief maps. Early-rift uplift is interpreted as a record of early-rift faulting with possible additional mantle support, whereas later uplift was driven by fault linkage and mantle upwelling (12-6 Ma) as well as transform tectonics (6-0 Ma). These modeling results are largely in agreement with other independent data (low-temperature thermochronology and dated carbonate terraces). Our workflow benefits from its utilization of ubiquitous drainage data. The combination of drainage analysis and inverse modeling proves to be more discerning than either one method in isolation, and may have application to analysis of other margins.

Keywords: Continental uplift; Drainage analysis; Stream profile modeling.

1. Introduction

Estimating the uplift of rift flanks and passive margins has been a subject of several studies, given its importance for understanding the evolution of continental margins (e.g., Japsen et al., 2012; Weissel & Karner, 1989). Different processes have been proposed to explain elevated rifted margins, focusing on uplift timing vis-à-vis rifting. Several authors have attributed uplift directly to rifting, where processes including mechanical unloading during extension (Weissel & Karner, 1989) and extensional faults on the flanks of transform boundaries (e.g., the Gulf of Aqaba; Bosworth et al., 2017) are invoked. Others have demonstrated the relative youth of such uplifts, suggesting post-rift processes (e.g., West Africa; Doglioni et al., 2003; Walford & White, 2005; West Greenland; Japsen et al., 2012). Other models invoke no direct relation between rifting and uplift (e.g., the Norwegian margin; Osmundsen & Redfield, 2011), in which case other processes are reported to drive uplift (e.g., lithospheric unloading due to differential denudation; Gilchrist & Summerfield, 1990).

Uplift has an impact on the evolution of drainage catchments and streams. This makes landscape characterization a valuable tool to study the spatio-temporal evolution of uplift (e.g., Twidale, 2004). The use of longitudinal river profiles (i.e., elevation vs. distance to base-level) to reconstruct epeirogeny-related uplift histories, in particular, has recently received considerable attention (e.g., Paul et al., 2014; Roberts & White, 2010; Wilson et al., 2014).

The effect of uplift on the landscape, however, may be difficult to interpret where significant variations in climate and rock strength affect the landscape, especially at scales < 100 km (Wapenhans et al., 2021; Whipple et al., 2017). Landscape evolution in response to climate change has been discussed in the literature. For instance, in wetter climates an increase in discharge downstream might increase stream power and incision rates (Wobus et al., 2010). Substrate strength and contrasts have also been suggested as an important means for generating relief along river profiles (e.g., Bursztyn et al., 2015; Gallen, 2018). Spectral analyses of North American river profiles indicate that changes in substrate likely contribute a few percent to the geometries of longitudinal river profiles and are increasingly important contributors at short wavelengths (< 100 km; Wapenhans et al., 2021). Wilson et al. (2014) showed that, at wavelengths > 5 km, the slopes of channels draining the Arabian Peninsula are weakly correlated with lithological contacts. Instead, they suggest that these changes in slope (i.e., knickzones) are generated by the history of uplift rate.

The northern Red Sea (Figure 1) is flanked by exposed Neogene rift basins, with an active transform at the Gulf of Aqaba (Bosworth et al., 2005). Topographically, the Arabian escarpment has an average elevation of ~1 km whereas on the African side elevations are ~400-600 m lower. Climate is presently mostly arid resulting in a lack of permanent rivers on the Arabian side that would have formed deltas in wetter paleo-climates such as during the Messinian Age (Bosworth, 2015; Griffin, 1999; Wilson et al., 2014).

Uplift and exhumation have been estimated at some locations around the northern Red Sea margins (Bosworth, 2015). Apatite fission track (AFT) data suggest denudation from 27 to 20 Ma in Sinai (Kohn & Eyal, 1981) and 23 to 21 Ma west of the Gulf of Suez (Omar et al., 1989). Across the Central Arabian Rift Flank (CARF), modeling of (U-Th)/He apatite and zircon data (AHe and ZHe) suggests the exhumation of ~1.7±0.8 km deep basement rocks across a 150 km-wide zone at ~23 Ma, before faulting migrated towards the central basin at ~15 Ma (Szymanski et al., 2016). East of the Gulf of Aqaba, transform tectonics resulted in a much younger uplift, as evidenced by the elevated positions of Pleistocene terraces (Bosworth et al., 2017).

Despite the aforementioned evidence, little work has been undertaken to constrain the Neogene uplift along subaerial parts of the northeastern Red Sea and the eastern Gulf of Aqaba. Here, the tectono-geomorphological evolution is investigated, to map uplift variation in the area. Uplift history is estimated through inverse modeling of longitudinal stream profiles. Analysis of the present-day drainage is undertaken to investigate the relationship between uplift and drainage evolution, which are presented in a tectono-geomorphological evolutionary model. This approach benefits from good spatial coverage and has applicability to other margins worldwide.

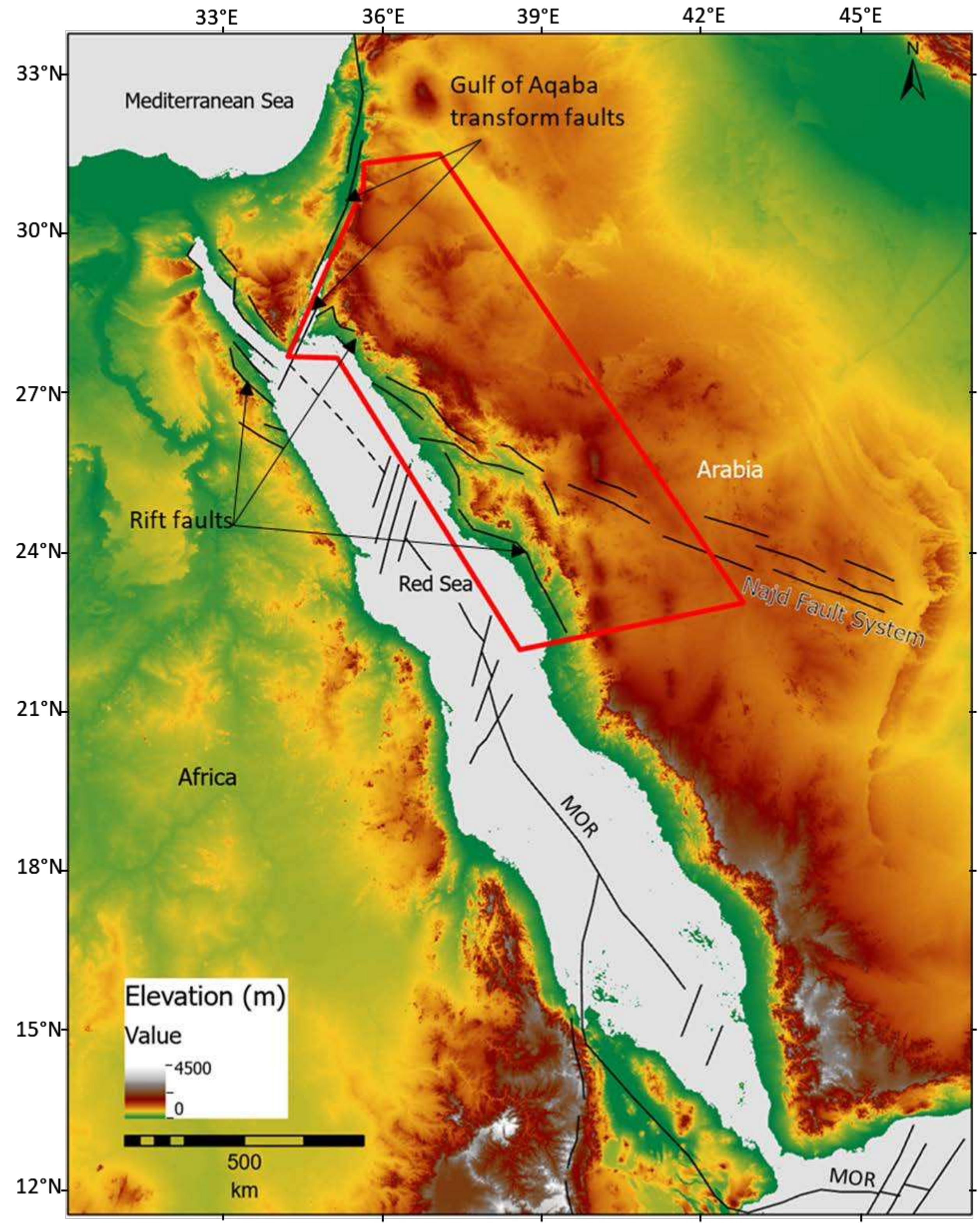

Figure 1: A Digital Elevation Model (DEM) topographic map of the areas surrounding the Red Sea showing the elevation variation along the Red Sea coast and escarpments. Black lines: faults and Mid-Ocean Ridge (MOR) (dashed where uncertain; compiled from Bosworth et al. (2005), Tubbs et al. (2014) and Szymanski et al. (2016)). Red polygon: extent of study area.

2. Geologic setting

Rifting across the Arabian-Nubia Shield commenced in the Oligo-Miocene times, producing ~20-30 km-long normal faults that likely reactivated Precambrian structures such as parts of the Najd Fault System (Figure 1; Bosworth et al., 1998; Bosworth et al., 2005; Gawthorpe et al., 1997). The early rifting phase was also associated with NNW-SSE striking basaltic dykes on the Arabian margin (~24 Ma; Hughes & Filatoff, 1995; Pallister, 1987). By the end of the Aquitanian period, fault segment linkage had been established (Bosworth & McClay, 2001).

Fault coalescence, relay ramp breaching and shoulder uplift continued in the Aquitanian-Burdigalian ages (Bosworth & McClay, 2001; Koeshidayatullah et al., 2016), leading to an angular unconformity at ~21 Ma (Tubbs et al., 2014), coeval with basinal accelerated subsidence (Steckler et al., 1988). This period lacked magmatism (19-13 Ma; Coleman et al., 1983) and featured strain migration towards the rift axis (Bosworth et al., 2005). Uplift was associated with normal faulting during the Late Oligocene-Early Miocene extension across a 150 km-wide zone of deformation (Szymanski et al., 2016). In a synthesis of published low-temperature thermochronological data, Bosworth (2015) concluded that denudation of the footwall blocks around the Red Sea commenced between 24-23 Ma and the regional rift shoulders developed by 22-20 Ma.

Postdating the subsidence, another unconformity surface signifies plate-scale stress reorganization prior to the Gulf of Aqaba strike-slip activity (Bosworth et al., 2005; Tubbs et al., 2014). Between 14-12 Ma, deformation along the future transform commenced as extension directions became NNE-SSW (Bosworth et al., 2005). Coevally, N-S-oriented transitional-alkalic volcanism (implying mantle upwelling influence) occurred on the Arabian side (12 Ma; Camp & Roobol, 1992, and 13 Ma; Ilani et al., 2001).

Deformation intensified along the Gulf of Aqaba during the Pliocene epoch, coeval with seafloor spreading (5 Ma) in the southern Red Sea and continental extension and signs of early oceanization further north (Bosworth et al., 2005; Cochran, 2005). Uplift along the Gulf is evidenced by elevated Pleistocene marine coral terraces that, when global sea-level drop is taken into consideration, suggest an average uplift rate of 0.15 mm/a since 125 ka (Bosworth et al., 2017). The time-equivalents of these marine terraces along the Red Sea have not been uplifted (Plaziat et al., 1998).

Tectonic, magmatic and geomorphic changes, which accompanied rifting, have been described from several locations along the Red Sea, Gulf of Suez and Gulf of Aqaba, and they indicate a general northward paleo-drainage direction prior to, and during, the early rifting phase. Anvi et al. (2012) suggested a regional-scale northward topographic slope at western Arabia and northeastern Africa during the Oligocene epoch. This slope would likely have been an important control on the drainage direction (e.g., Brown et al., 1989). Furthermore, sedimentological observations from the Levant suggest that the Early Miocene sediments were at least partly supplied from south (i.e., northward river direction; Zilberman & Calvo, 2013).

3. Methodology

Geomorphic analyses were performed here to establish the tectono-geomorphic evolution of uplifted margins using ~30 x 30 m-horizontal resolution Advanced Spaceborne Thermal Emission and Reflection Radiometer global digital elevation model (ASTER GDEM is a product of NASA and METI; https://gdex.cr.usgs.gov/gdex/). The data cover the drainage catchments that have their outlets at the coastline of the northeastern Red Sea and eastern Gulf of Aqaba (Figure 1). ArcMap was used to extract drainage networks from the DEM following the D-8 flow routing procedure (O'Callaghan & Mark, 1984; Tarboton et al., 1991).

3.1. Drainage inverse modeling

Geomorphic metrics, such as normalized steepness indices (k_{sn}) or chi-elevation integral analyses, are widely used to constrain histories of landscape evolution (e.g., Kirby & Whipple, 2012; Perron & Royden, 2013; Snyder et al., 2000; Whipple & Tucker, 1999). A challenge with using such approaches is that one is forced to assume that rivers are at steady state or that the functional form of uplift is known a priori. Alternatively, inverse approaches have been used to solve the stream power model to calculate temporal and spatio-temporal uplift histories (see e.g., Goren et al., 2014; Paul et al., 2014; Pritchard et al., 2009; Roberts & White, 2010; Roberts et al., 2012; Rudge et al, 2015).

Here, the inverse approach of Rudge et al. (2015) was used to calculate the uplift history of the northern Red Sea and eastern Gulf of Aqaba onshore margins. The equation describing the relationship between uplift, erosion and profile shape is given by:

$$\frac{\partial \mathrm{z}}{\partial \mathrm{t}} = \mathrm{U}(x, t) - \mathrm{E}(x, t) \tag{1}$$

where U and E are the rates of uplift and erosion, respectively. $\partial \mathrm{z}/\partial \mathrm{t}$ is the rate of change of elevation with time, and x is the distance along the river (e.g., Roberts & White, 2010; Whipple & Tucker, 1999; Wilson et al., 2014). It is generally accepted that the stream power erosional model provides a practicable way of modeling longitudinal river profile evolution on long length and time (more than 1 Myrs) scales (e.g., O'Malley et al., 2021; Roberts et al., 2019; Rosenbloom & Anderson, 1994; Whipple & Tucker, 1999). The erosional model includes advection (i.e. kinematic waves of erosion propagating upstream) and erosional 'diffusion' (e.g., Rosenbloom & Anderson, 1994; Whipple & Tucker, 1999) so that:

$$E = -vA^m \left(\frac{\partial \mathrm{z}}{\partial x}\right)^n + \kappa \left(\frac{\partial^2 \mathrm{z}}{\partial x^2}\right), \tag{2}$$

where n and m are dimensionless positive exponents of the stream gradient ($\partial \mathrm{z}/\partial \mathrm{x}$) and upstream area ($A$), respectively. The prefactor v determines advective velocity when $n=1$ and $m=0$, and κ is a 'diffusion' constant. A^m is a proxy for discharge and n and m control profile concavity.

To solve for uplift rate, erosional parameters must first be calibrated. Here, the v and m values are set to 120 $\mathrm{m}^{0.6}$ /Myr and 0.2, respectively. These values were calibrated by Wilson et al. (2014) from the history of incision of radiometrically-dated lava flows of Harrat Rahat, which lies partially within the southern part of our study area. κ can vary by many orders of magnitude without significantly affecting calculated uplift histories (e.g., Rosenbloom & Anderson, 1994). Following Wilson et al. (2014), Equation 1 is simplified to a linear version of stream power model in which $n = 1$ and $\kappa = 0$ such that:

$$\frac{\partial \mathrm{z}}{\partial \mathrm{t}} = U(\mathrm{t}) - vA^m \left(-\frac{\partial \mathrm{z}}{\partial x}\right). \tag{3}$$

Rearranging using the method of characteristics and integrating (using present-day values of x and z as boundary conditions at $t = 0$, and $x = 0$ and $z = 0$ as boundary conditions at a time in the past), this equation can be rewritten as:

$$z^* = \int_0^{\tau_G} U(x(t), t)dt \quad (4)$$

$$\tau_G = \int_0^{x^*} \frac{dx}{vA^m} \quad (5)$$

and

$$\tau_G - t = \int_0^{x(t)} \frac{dx}{vA^m} \quad (6)$$

where z^* and x^* are the present-day elevation and distance, respectively. τ_G is the landscape response time to an erosional signal propagating upstream (e.g., from $x = 0$; Rudge et al., 2015).

Equations 4-6 can be used to invert longitudinal river profiles for spatio-temporal uplift rate histories (U). In this paper, uplift rates are defined on a spatial grid with vertices 10-15 km-apart and time steps of 1 Ma. Uplift rates are then linearly interpolated between these vertices at each time step to build uplift rate maps. Integration of uplift rates with respect to time, $\int Udt$, gives cumulative rock uplift.

The horizontal positions, elevations and upstream drainage areas were extracted along longitudinal profiles of rivers (bed elevation vs. distance from outlet; Figure 2). The profiles were jointly inverted, whereby the model iteratively compares actual river shapes with predicted profiles. We seek the smoothest uplift rate history that minimizes the misfit between the two.

Changes in sea-level during the Neogene period, and associated changes to the length of rivers as more or less of the continental shelf was exposed, are unlikely to have affected calculated uplift rate histories substantially (Wilson et al., 2014). Therefore, for simplicity, we assume that base-level was constant across the study area. If this eustatic sea-level drop signal has an effect on the modeled uplift rate maps, it is expected to have had the same effect on all of the study area. It is also noted that the amount of average sea-level drop around Arabia since the start of the Miocene epoch is ca. 150 m (Haq & Al-Qahtani, 2005), which is an order of magnitude smaller than calculated uplift.

Landscape response times calculated using calibrated erosional parameter values indicate that pre-Miocene events are likely to be poorly resolved (Figure 10 in Wilson et al., 2014). We note that geologic evidence, including marine sedimentary rocks and laterites overlain by Oligocene basalts, indicates that much of Arabia was likely characterised by subdued topography and shallow submergence during Late Mesozoic-Early Cenozoic times (e.g., Bohannon et al., 1989; Burke & Gunnell, 2008; Wilson et al., 2014). O'Malley et al. (2021) showed that precipitation rate variations with frequencies of order 1 Ma or less do not generate significant changes in calculated stream profiles. For simplicity we start by assuming constant precipitation rates and return to this issue later.

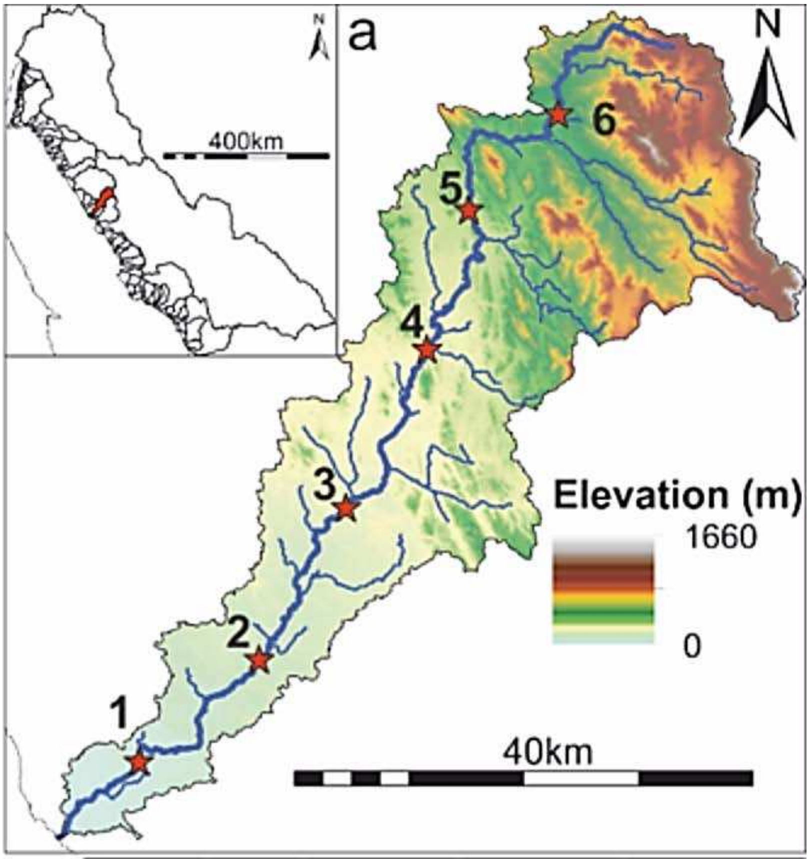

b

Point	X (long.) (m)	Y (lat.) (m)	Z (elevation) (m)	x (distance from divide) (m)	A (upstream drainage area) (m^2)
1	-1128732	165174	34	120038	1277613562
2	-1117442	172752	103	100002	1178018800
3	-1108522	184884	176	80003	991023182
4	-1100039	197640	242	60038	699123195
5	-1095112	209148	305	40024	429141506
6	-1086535	216477	431	20023	127177679

Figure 2: An example of the drainage data used in the inverse modeling to estimate uplift rates. a) A DEM (ASTER GDEM) map of one catchment (see inset for location) showing the stream network and points (red stars 1-6) where data were extracted for modeling. ASTER GDEM is a product of NASA and METI. b) The data extracted for each point (i.e., X, Y, Z, distance along stream and upsteam drainage area). The points are only examples and the actual dataset is much denser (~30-43 m-apart).

Substrate lithology in the study area is variable and encompasses igneous, metamorphic and sedimentary units (Figure 3). Nonetheless, the effect that lithological variation has on the input to the inverse modeling (i.e., the stream profile shapes) appears to be minimal (Figure 4). The notable exception is where catchment NERS4 main stream crosses the escarpment. We, therefore, start by assuming that erosional parameter values (*v, m*) are constant.

The assumption that river network planforms are static is often used as a starting point to infer the control of tectonics, climate and eustatic sea-level change on the topography. In contrast, some studies suggest that drainage divide migration can be an important means of modifying landscapes (e.g., Willett et al., 2014). Here, as a starting point the network is assumed to be static, we then examine how drainage reorganization might impact evolution of the fluvial network using guided forward models.

3.2. Landscape evolution forward modeling

Simulators capable of predicting landscape evolution at continental scales, with variable precipitation, planforms and substrate erodibilities, have recently been developed (e.g., Landlab: Hobley et al., 2017; Badlands: Salles and Hardiman, 2016). Using these models to invert for uplift histories, which can require $O(10^6)$ iterations, at continental scales is currently prohibitively expensive. Nonetheless, we can test the impact of changing precipitation, planforms and starting conditions by making use of a closed-loop modelling strategy (O'Malley et al., 2021). In this strategy, first, longitudinal river profiles were inverted to calculate the uplift rates histories using the model described in the previous section. Secondly, the calculated histories were used to drive forward model simulations of landscape evolution using the Badlands libraries (Salles & Hardiman, 2016). These models allow drainage networks to evolve dynamically under a range of precipitational histories. Thirdly, river profiles are extracted from the 'modern' simulated landscapes and inverted for an uplift rate history, which can then be compared with results generated by inverting Arabia's actual river profiles using the relatively simple erosional model (e.g. constant precipitation, fixed planforms). In this way, we can examine the impact of changing model parameters on calculated uplift patterns.

Geomorphic and sedimentological observations and interpretations (e.g., Anvi et al., 2012; Brown et al., 1989; Zilberman & Calvo, 2013) indicate that the pre-rift drainage was directed in general towards the north. As a separate test, we therefore, examine the impact of initiating models with flat-lying and north-dipping different initial topographies. The results of this exercise are discussed later when evaluating the inverse modeling (Discussion section).

3.3. Local relief and minimum erosion estimate

Cumulative uplift distribution can lead to erosion variation in space (e.g., Forte and Whipple, 2018). It can, therefore, be compared against the topography in terms of local relief and minimum erosion magnitude. Using DEM data, local relief and the minimum erosion maps were constructed. The local relief was computed with an average window of 10 x 10 km cells by calculating the difference between the maximum and minimum elevations within each cell.

A minimum erosion height map was constructed by subtracting the present-day topography from a surface connecting the interfluve elevations within the catchments. This latter surface is assumed here to represent the elevation of the pre-incision (pre-rift) surface. A similar methodology was followed to assess erosion variation in tectonically active regions (e.g., Bellin et al., 2014; Giaconia et al., 2012). For each drainage catchment, the estimated erosion heights were summed to yield a minimum erosion volume. To normalize the minimum erosion volume between the catchments, its values were divided by the corresponding catchments' areas to find the ratio of volume-to-area (R_{va}), which makes a comparison between the catchments possible. This approach is simplistic and subject to uncertainty in terms of the exact height of erosion. Here minimum erosion maps were used to understand the relative spatial distribution of erosion.

4. Results

4.1. Geomorphic characterization

Arabian drainage catchments emptying into the northern Red Sea and the Gulf of Aqaba are shown in Figure 3. Topographically, the onshore margin can be divided into high-elevation southern and northern zones separated by a low-elevation area (Figure 3a). Two *c.*100 km-wide swatch profiles capture clearly the topographic variation between these zones (Figure 5). The DEM map and swath profiles show a discontinuous mountain range in the south with an average elevation of ~650 m, and a more continuous escarpment with an average elevation of ~1100 m in the north (Figure 5). The drainage divide coincides with the top of the escarpment where clearly mapped, except at catchments NERS1 and 4 and parts of NERS11 (Figures 3 and 5).

As indicated in the Methodology section, only Red Sea catchments with sizes larger than 200 km^2 are considered in this study. Those catchments have a variable range of sizes with mean values of 1,400 km^2 (northern zone) and 1,100 km^2 (southern zone; Figure 3b). The catchment in between (i.e., NERS20) has a significantly larger area of ~105,000 km^2.

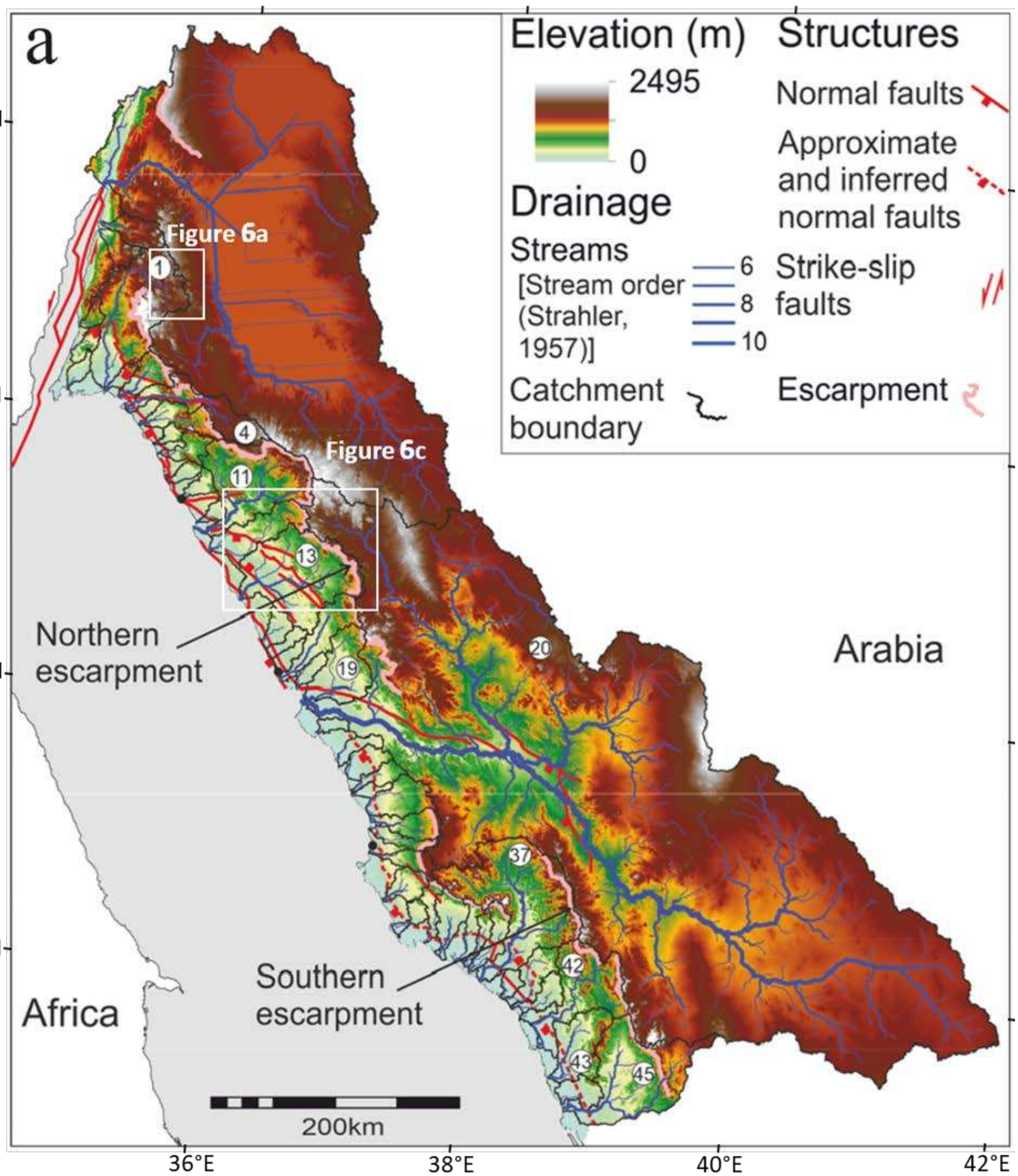
a
Elevation (m)
2495
0
Structures
Normal faults
Approximate and inferred normal faults
Strike-slip faults
Escarpment
Drainage
Streams
[Stream order (Strahler, 1957)]
6
8
10
Catchment boundary
Figure 6a
Figure 6c
1
4
11
13
19
20
37
42
43
45
Northern escarpment
Southern escarpment
Arabia
Africa
200km
30°N
28°N
26°N
24°N
36°E
38°E
40°E
42°E

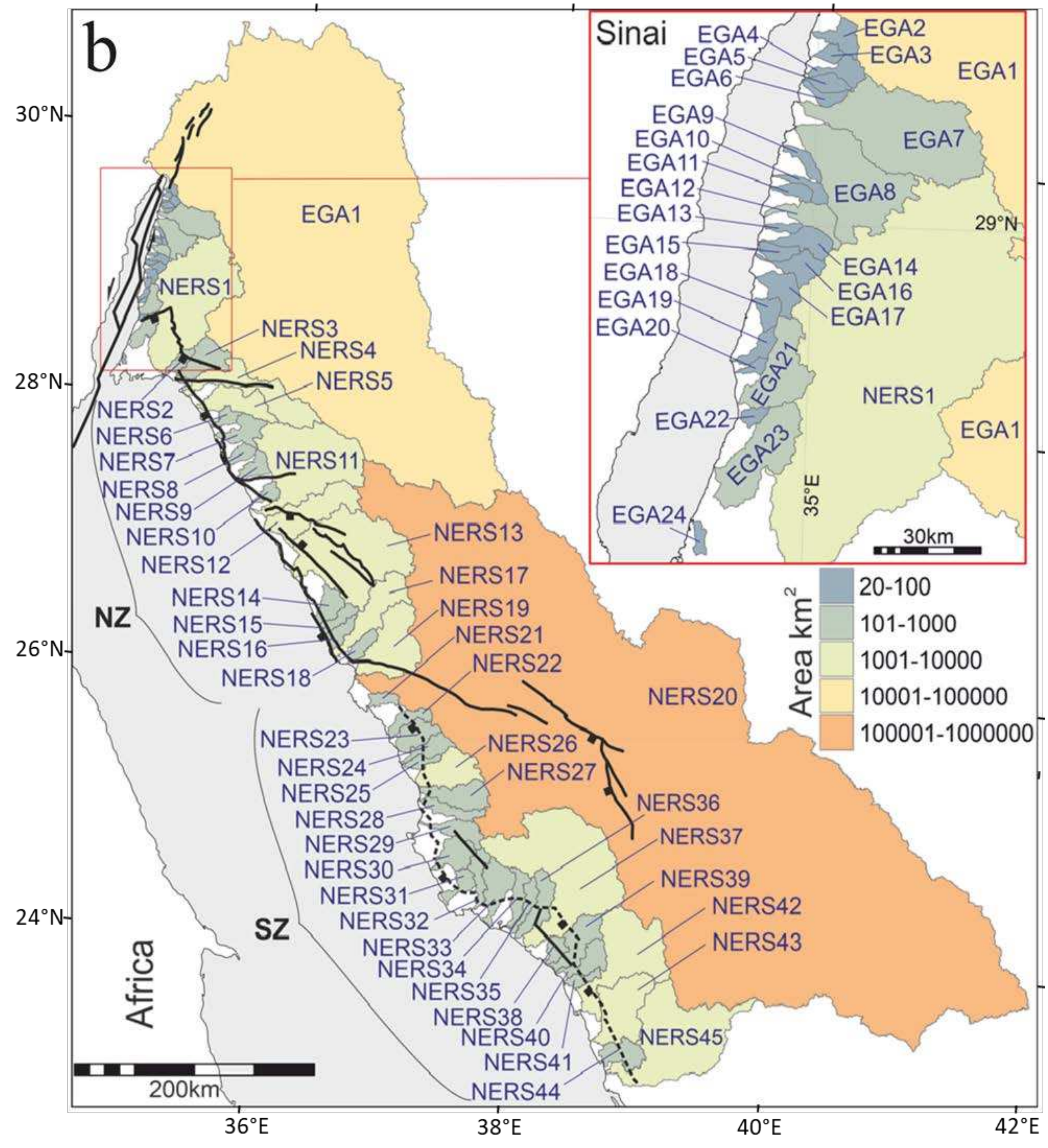
b
Sinai
EGA1
EGA2
EGA3
EGA4
EGA5
EGA6
EGA7
EGA8
EGA9
EGA10
EGA11
EGA12
EGA13
EGA14
EGA15
EGA16
EGA17
EGA18
EGA19
EGA20
EGA21
EGA22
EGA23
EGA24
29°N
35°E
30km
NERS1
NERS2
NERS3
NERS4
NERS5
NERS6
NERS7
NERS8
NERS9
NERS10
NERS11
NERS12
NERS13
NERS14
NERS15
NERS16
NERS17
NERS18
NERS19
NERS20
NERS21
NERS22
NERS23
NERS24
NERS25
NERS26
NERS27
NERS28
NERS29
NERS30
NERS31
NERS32
NERS33
NERS34
NERS35
NERS36
NERS37
NERS38
NERS39
NERS40
NERS41
NERS42
NERS43
NERS44
NERS45
NZ
SZ
Africa
200km
Area km^2
20-100
101-1000
1001-10000
10001-100000
100001-1000000
30°N
28°N
26°N
24°N
36°E
38°E
40°E
42°E

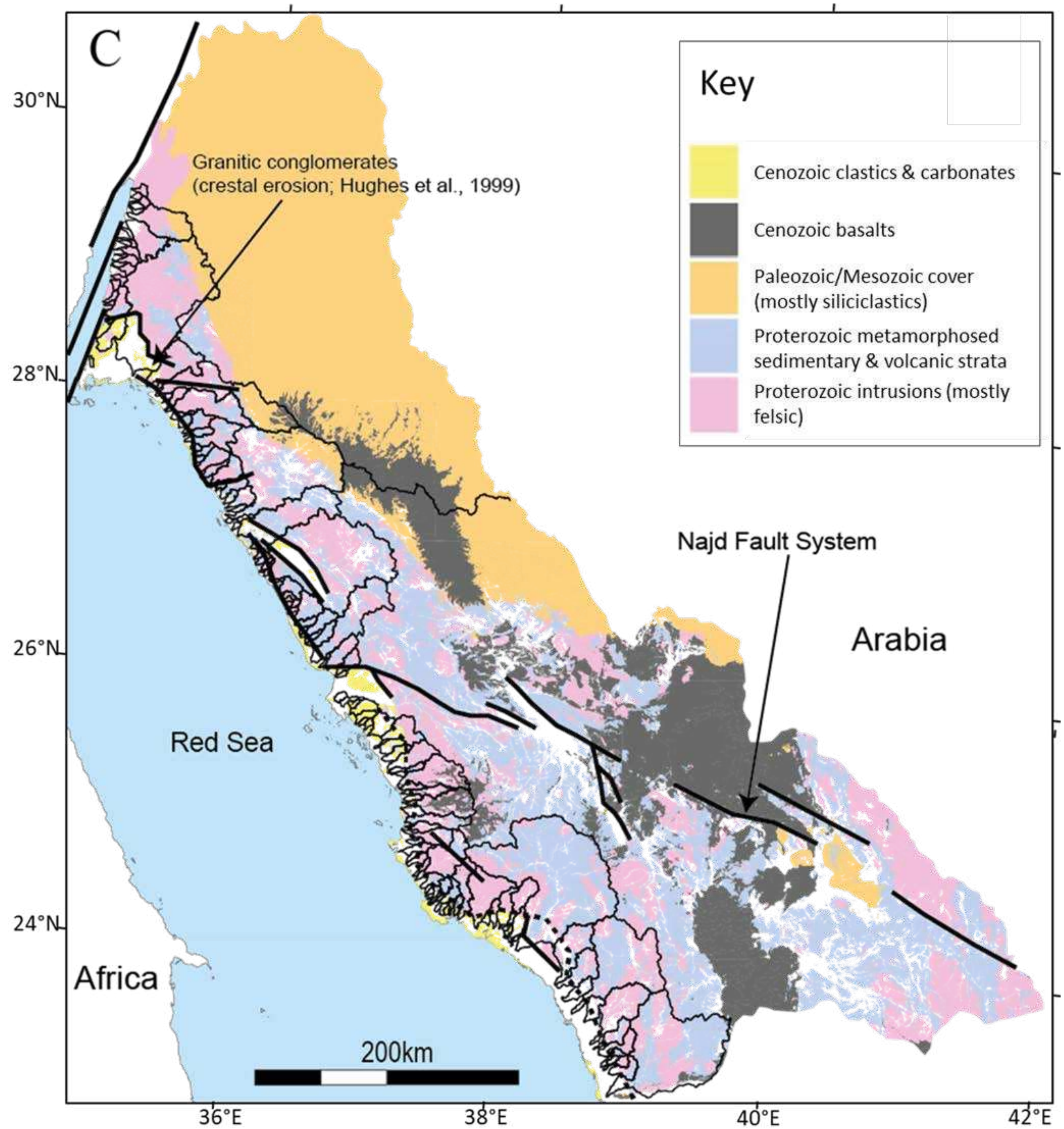

Figure 3: Topography, drainage and geology of the study area. a) ASTER GDEM map showing the drainage network and catchments. Faults are compiled from Brown et al. (1989), Tubbs et al (2014) (northern zone), and Szymanski et al. (2016) (southern zone). Circled numbers = selected NERS catchments for reference. b) Catchment sizes for the northeastern Red Sea (NERS#; >200 km²) and eastern Gulf of Aqaba (EGA#; >20 km²). c) Simplified geologic map showing drainage catchments (modified from Saudi Geological Survey (2016) and Powell et al. (2014)).

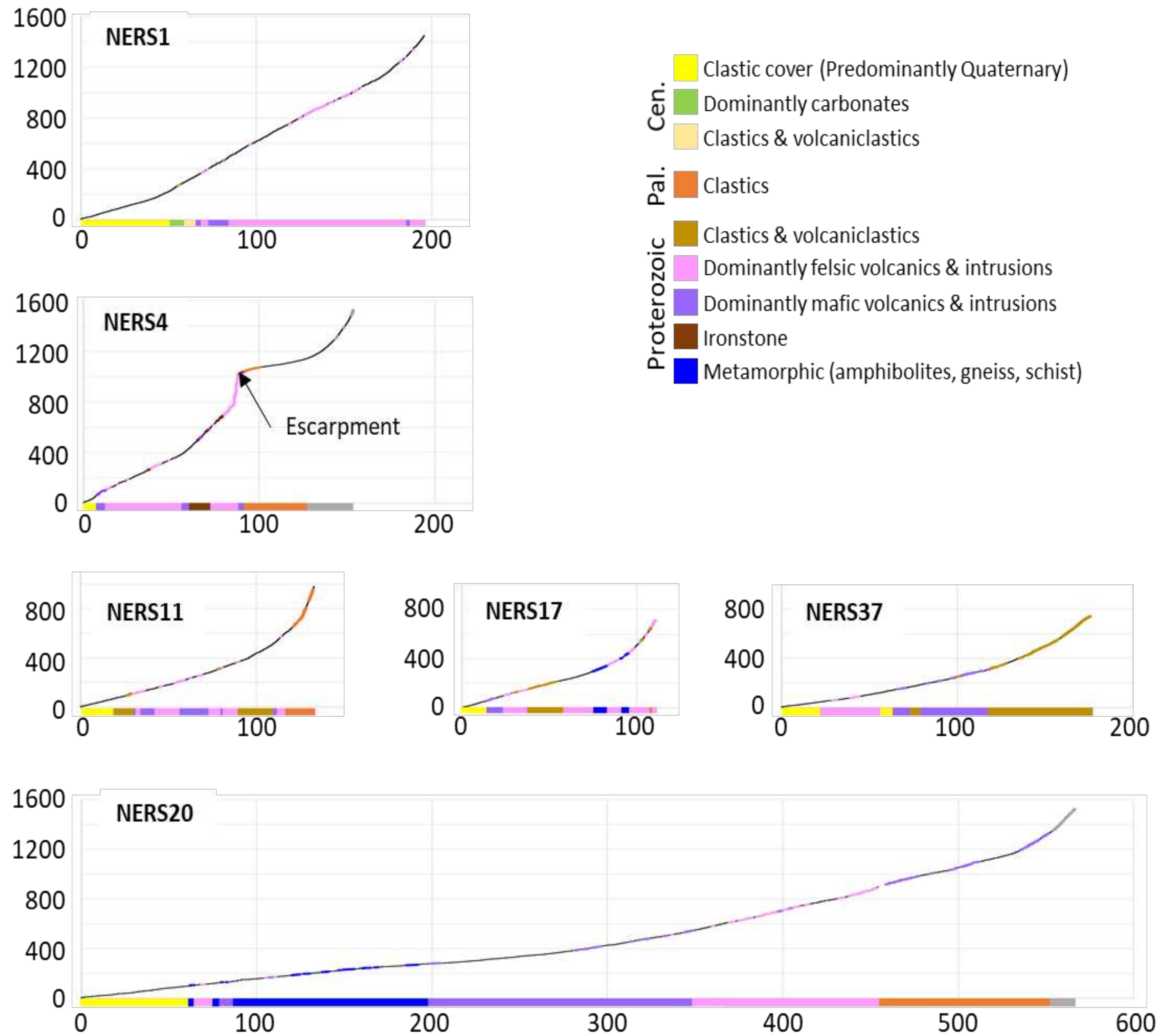

Figure 4: Main stream profiles extracted for selected Northeastern Red Sea catchments showing the main bedrock lithologies at the bottom of each panel (lithology modified from Saudi Geological Survey (2016)). These streams were used as inputs in the inverse modeling. Note that where the stream is covered by Quaternary clastics in upper sections the profile is colored in gray. Note that no km-scale change in profile slopes correlates with the lithology except at catchment NERS4 at the escarpment.

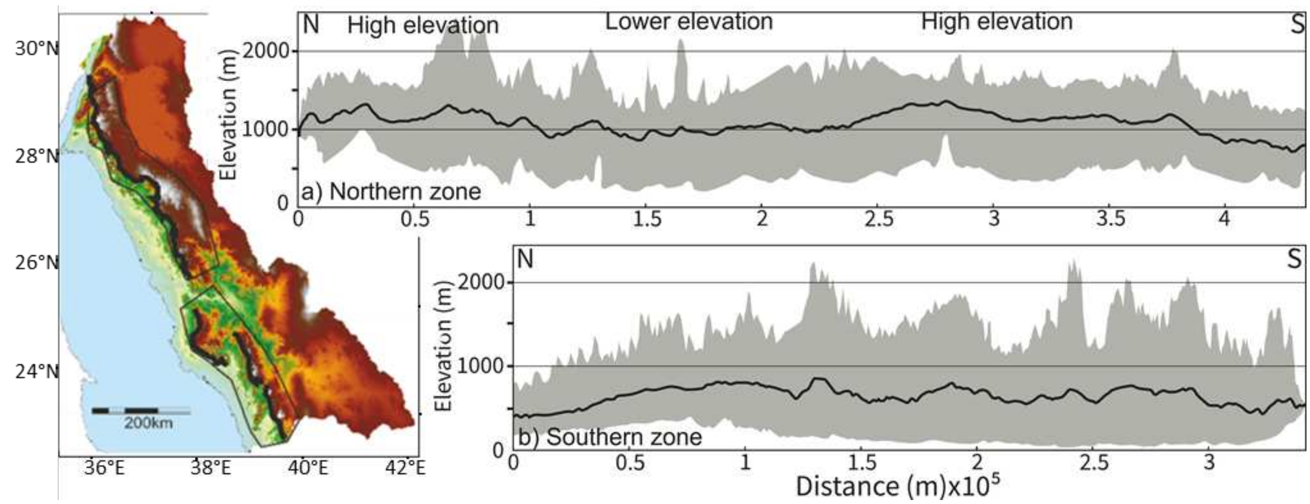

Figure 5: Black line = mean elevation, gray area = maximum and minimum elevation limits, along swath profiles of the escarpments. a) Northern zone. b) Southern zone. Locations of swaths are shown on the map (thin black outlines) and the escarpments are shown as thick black lines.

Approximately 100 km from the coast, NERS20's width increases dramatically from ~40 km to >700 km (Figure 3). Two main channel orientations are identified within NERS20; a NW-SE (semi-parallel to the Red Sea trend) and a WNW-ESE. West of the escarpments, the catchments that are <1000 km^2 are perpendicular to the coastline and ~90 km long in the south, becoming progressively shorter towards the NNW (~40 km; Figure 3). Catchment outlets are spaced at ~20-40 km intervals, with relatively short streams (generally <60 km) semi-perpendicular to the coastline. Larger catchments (1000 km^2-7000 km^2 in area), including NERS1, 4, 11, 13 and 37, have more irregular shapes that are narrow close to the coastline but wider away from it (Figure 3).

Along the Gulf of Aqaba, the elevation increases substantially to >1800 m (Figure 3a). The coastal plain widens gradually towards the north from very narrow (~3 km) to a maximum width of ~15 km, before narrowing again. Catchments along the Gulf with areas >20 km^2 have a mean area of ~130 km^2 excluding the regional EGA1 catchment (~59,000 km^2); remarkably smaller than catchments draining to the Red Sea (Figure 3b, inset box). The Gulf's catchments have axes that are perpendicular to its main axis. The exceptions are the catchments along the southern part of the gulf margin, which have more oblique shapes with long axes trending approximately 35° from the Gulf axis (e.g., EGA21 and 23; Figure 3b).

Drainage network planform of the study area is characterized mostly by a dendritic pattern. However, semi-linear trends of drainage streams stand out with respect to the overall dendritic pattern and characterize the network across catchment boundaries of NERS19, 17 and 13 (Figure 6c). Additionally, misfit streams are located east of the escarpments with NW-NNW and NE orientations in catchment NERS11, and at the boundary between catchments EGA1 and NERS1 (Figures 6a-b). As clearly shown on Figure 6a-c, although the streams are of low order, the valleys hosting them can be 0.5-1 km-wide.

Stream profiles (stream-bed elevation vs distance from outlet) have been extracted from Gulf of Aqaba catchments and northern Red Sea catchments (Figure 7). The observed NRS stream profiles are characterized by a general concave shape. Nonetheless, knickpoints exist along a few profiles, particularly in the northern part of the study area, spanning a distance from 70-160 km from the coastline (Figure 7b-c). In contrast, the Gulf of Aqaba stream profiles are more convex-shaped, with knickpoints and knickzones being within 40 km from the coastline (Figure 7a).

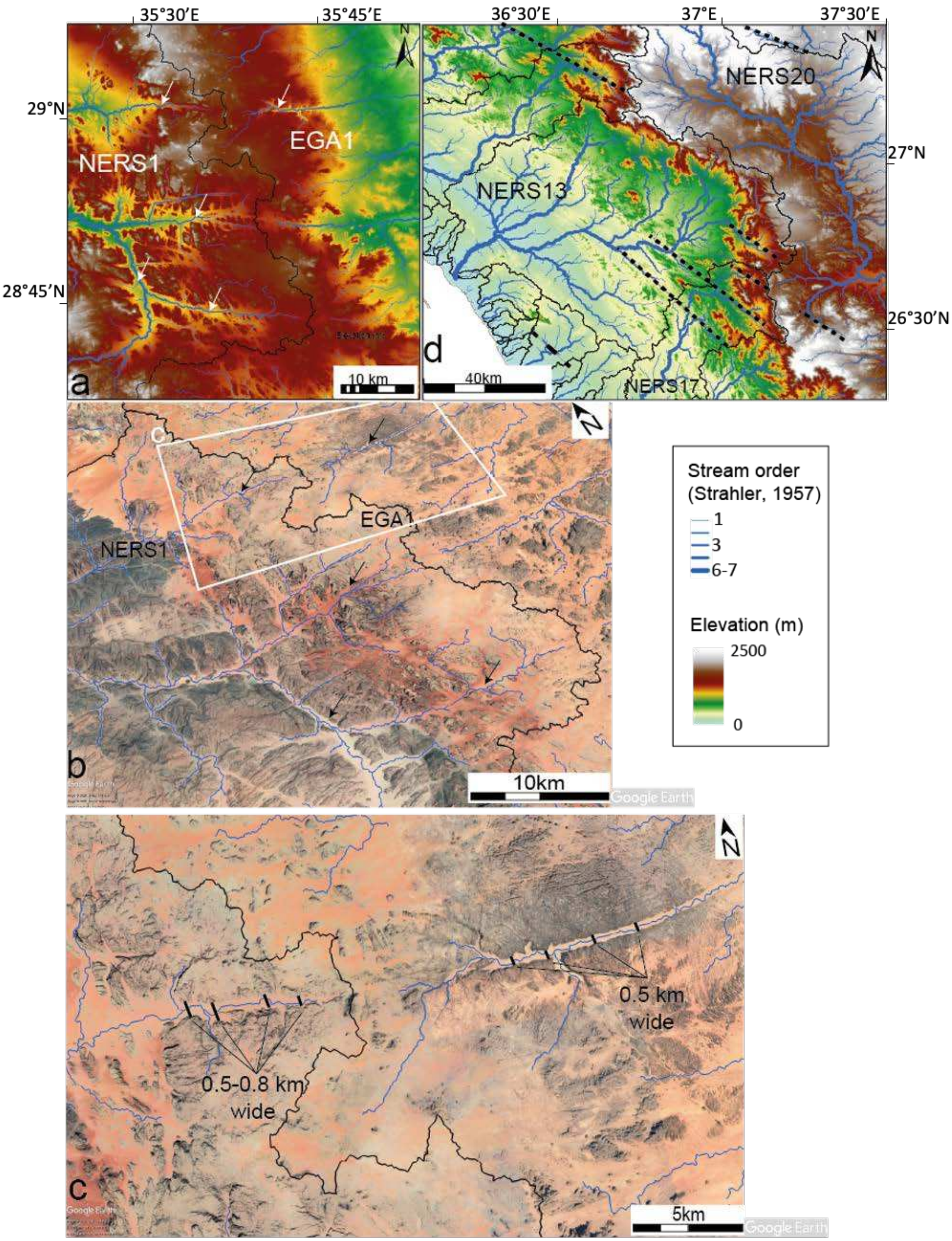

Figure 6: a) Drainage at the boundary between NERS1 and EGA1 showing examples of misfit streams (white arrows) where large valleys host low order streams. b) Bird's-eye view of the same extent of (a) showing the streams overlaid on a Google Earth image. Note the large valleys hosting the streams (black arrows). c) Close-up image of the Google Earth image in (b) showing detailed examples of misfit streams. Note location in (b). d) Drainage at NERS13 and surrounding catchments showing anomalously linear streams within and across catchments (indicated by black dashed lines). Refer to Figure 3a for locations.

4.2. Uplift estimation using inverse modeling

The best-fitting theoretical profiles fit the observed profiles well, with the exception of small misfits (~ ±50 meters) of headwater streams (Figure 7). The magnitudes of misfits between the observed elevations along the profiles and those modeled by the inverse algorithm cluster narrowly around zero (Figure 7e-g). Most of the misfits are located at the upper steep reaches of streams in the northern part of the study area west of the escarpment (Figure 7e-g).

The model predicts early uplift in the southern part of the study area that later shifted northward with minimal uplift in central areas (i.e., NERS20; Figure 8). Between 21-15 Ma, calculated uplift was distributed over an area >150 km wide with an average rate of ~0.14 mm/a (Figure 8b). During this period, the uplift wavelength became narrower from ~200 km (21 Ma) to ~120 km (15 Ma).

Starting at ~12 Ma, calculated uplift shifted northward, becoming focused with wavelengths of ~60 km and an average rate of ~0.14 mm/a (Figure 8b). Longer wavelength uplift is observed at the northwestern part of Harrat Uwayridh/ar Rahah, with a wavelength of ~100-120 km and an average rate of ~0.1 mm/a (9 Ma). During this period, ~60 km-wide uplift initiated along the eastern Gulf of Aqaba, narrowing down to ~20 km (6 Ma). Starting at ~3 Ma, zones of focused uplift (~20-60 km-wide) became dominant at the northernmost blocks (0.36-0.29 mm/a; Figure 8b). Presently, those zones are flanked by a ~200 km-wide zone of more diffuse uplift, with an average uplift rate of ~0.17 mm/a.

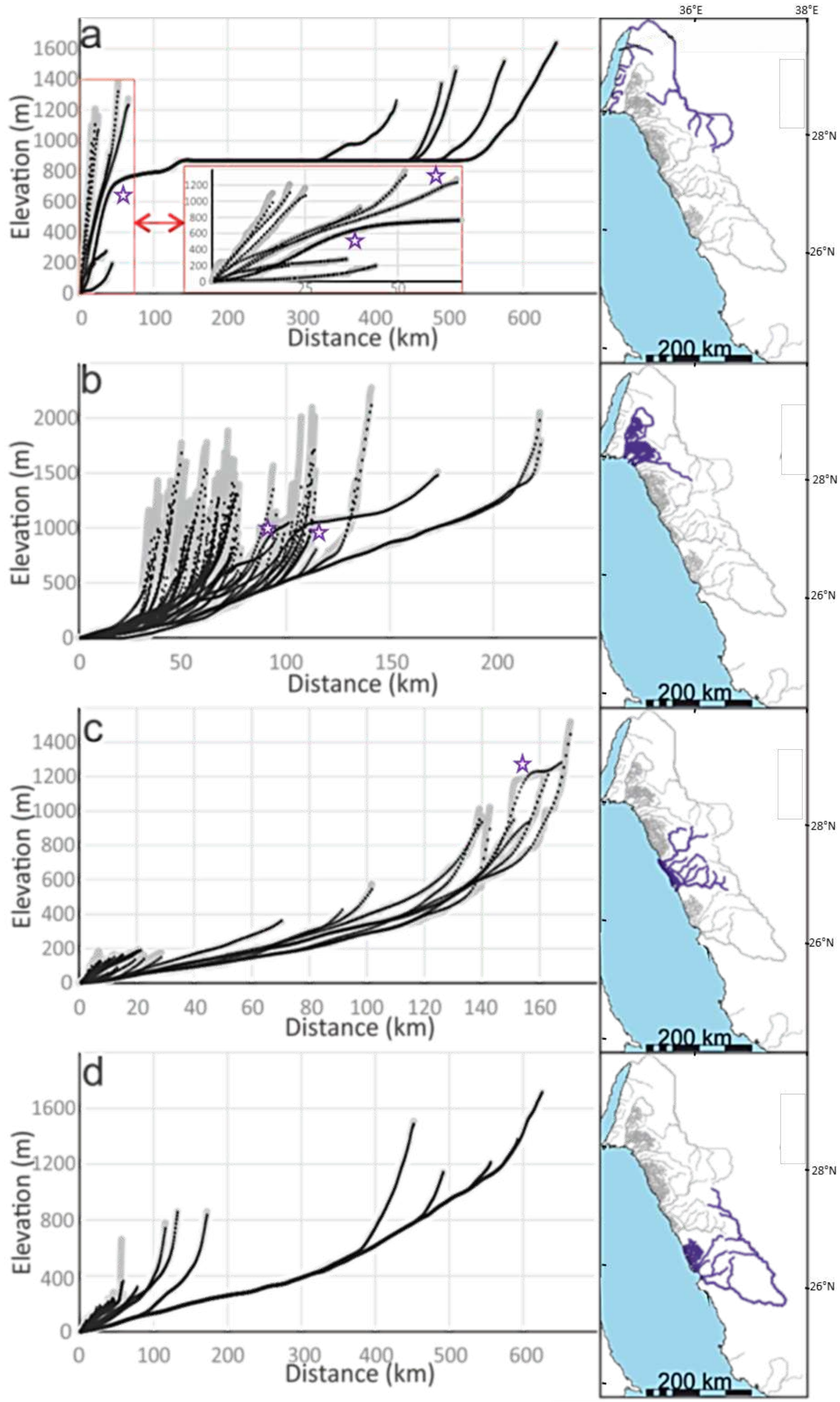

343

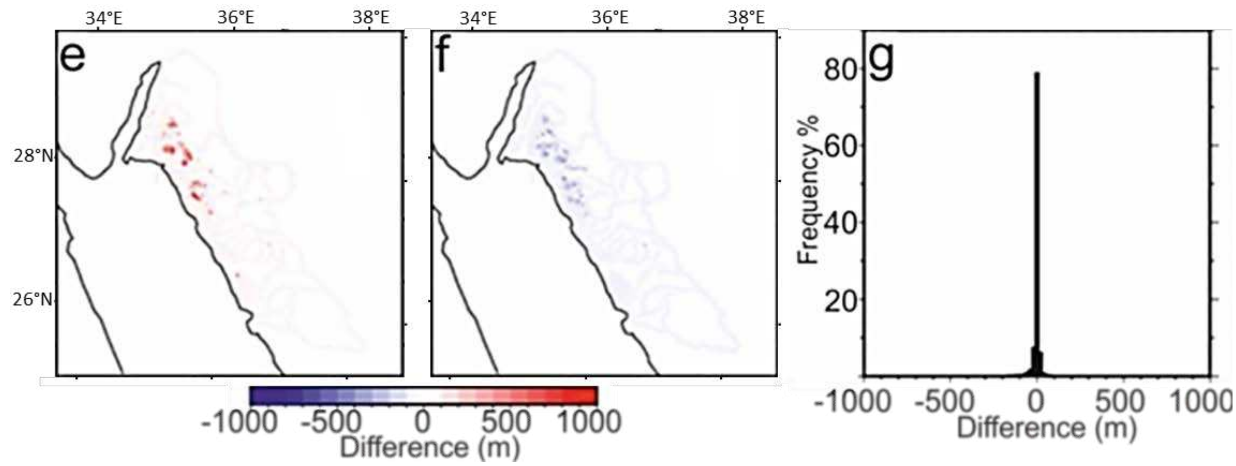

Figure 7: (a-d) Left: Extracted profiles (gray solid lines) and modeled profiles (black dotted lines) generated by the inverse model for (a) the Gulf of Aqaba streams and (b-d) the northern Red Sea streams. Note that the horizontal distances along the panels are different. Right: Corresponding locations of streams (blue lines). Note that the Gulf of Aqaba streams are generally convex-shaped (a) whereas the northern Red Sea streams are generally concave-shaped (b-d). Knickpoints and knickzones (purple stars) are observed along both Gulf of Aqaba and northern Red Sea stream profiles (a-c). (e-g) The misfit between the observed and theoretical profiles. (e) Residual positive misfit map. (f) Residual negative misfit. (g) Histogram of residual misfit, showing that the misfits cluster around zero difference.

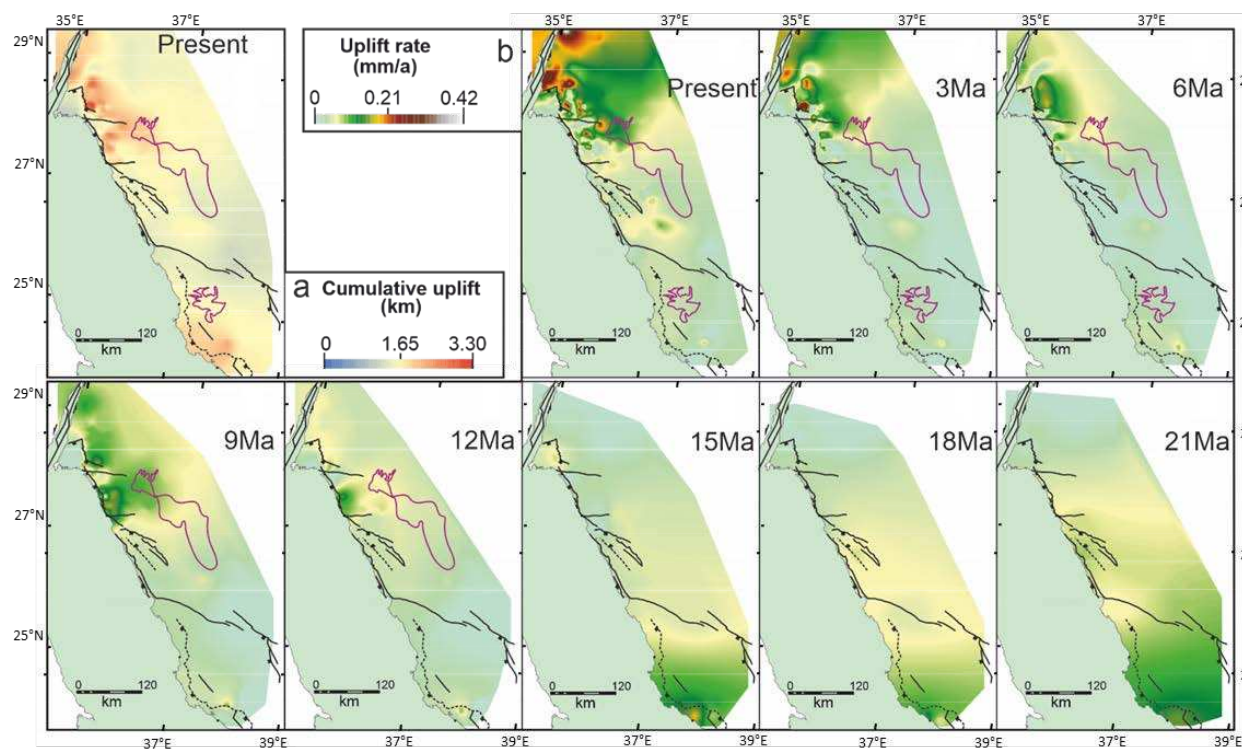

Figure 8: Uplift estimation from the stream profile inverse modeling. a) Estimated cumulative rock uplift magnitude at present-day. Note the two areas of uplift in the northern and southern part of the study area. b) Estimated uplift rates maps starting from 21 Ma until the present-day. Note that uplift in the southern area is estimated to have occurred earlier than the northern area. Faults (black lines) and volcanic fields (purple) are shown.

4.3. Minimum erosion volume and local relief estimation

The location of greatest erosion varies, becoming both more confined and closer to the coast towards the north with time (Figure 9). In the south, erosion is spread across a 60-80 km wide area that is, on average, ~60 km away from the coastline (Figure 9a). Further north erosion becomes focused on a 20-40 km-wide area 0-30 km away from the coastline. The catchment area plays a crucial role in the minimum erosion volume (e.g., catchment NERS20; ~5400 km^3; Figure 9b). Dividing the volume by the area yields high R_{va} values in the northern and southern zones compared to the central catchments (Figure 9c).

A 50-100 km wide belt of high relief runs parallel to the coastline, and is separated from it by a lower relief area (Figure 10). In detail, the local relief map shows similarity to the R_{va} map with both southern and northern zones of high values (Figures 9 and 10). A 50-100 km wide belt of high local relief is observed parallel to the coastline throughout the study area (Figure 10). Local relief drops rapidly between this belt and the coastline to values reaching zero within each 10 x 10 km window of observation.

Moderately positive spatial correlation is noted between these geomorphic observations and the estimated uplift from the inverse modeling of drainage profiles. The southern and northern zones of relatively high relief and R_{va} values coincide with the high cumulative rock uplift values described earlier (Figures 8a, 9c and 10).

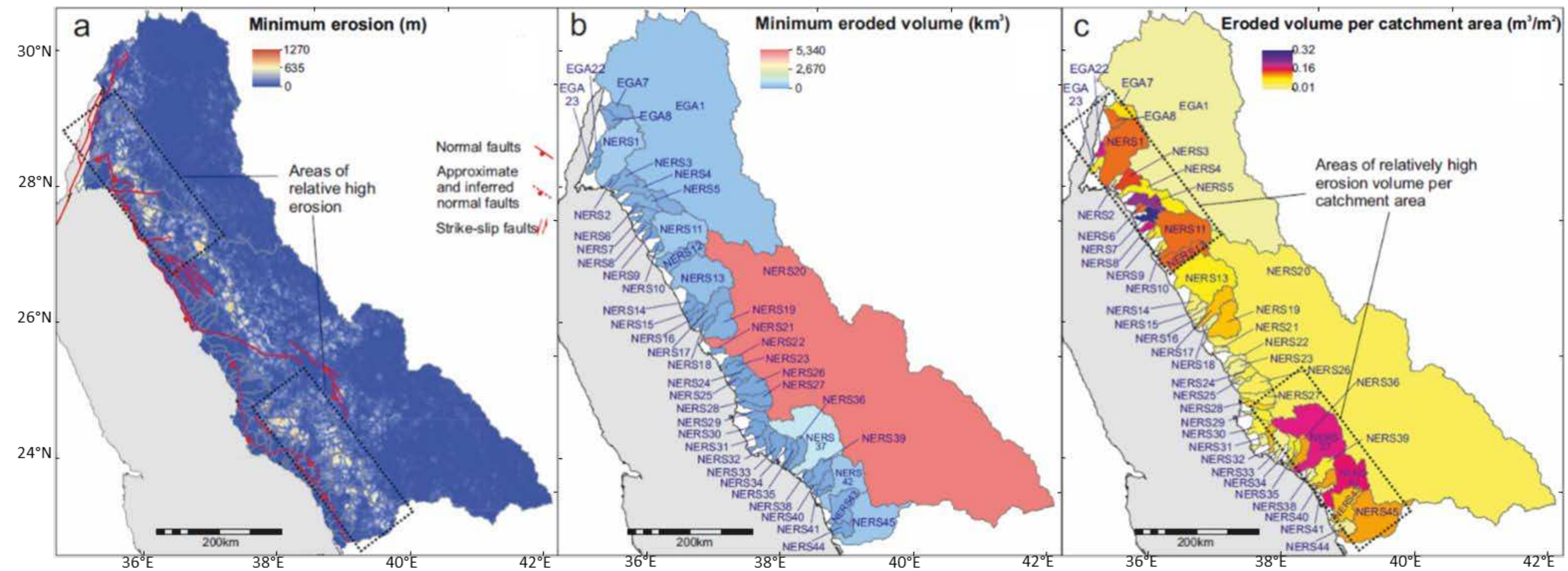

Figure 9: Erosional volume across the study area. a) Minimum erosion map produced using interfluve elevations to construct pre-erosion topography. b) Catchments draining to the Red Sea (NERS#) and Gulf of Aqaba (EGA#) with areas >200 km^2 , showing the contribution of eroded volume from each catchment. c) Volume:area ratios (R_{va}) values for each catchment.

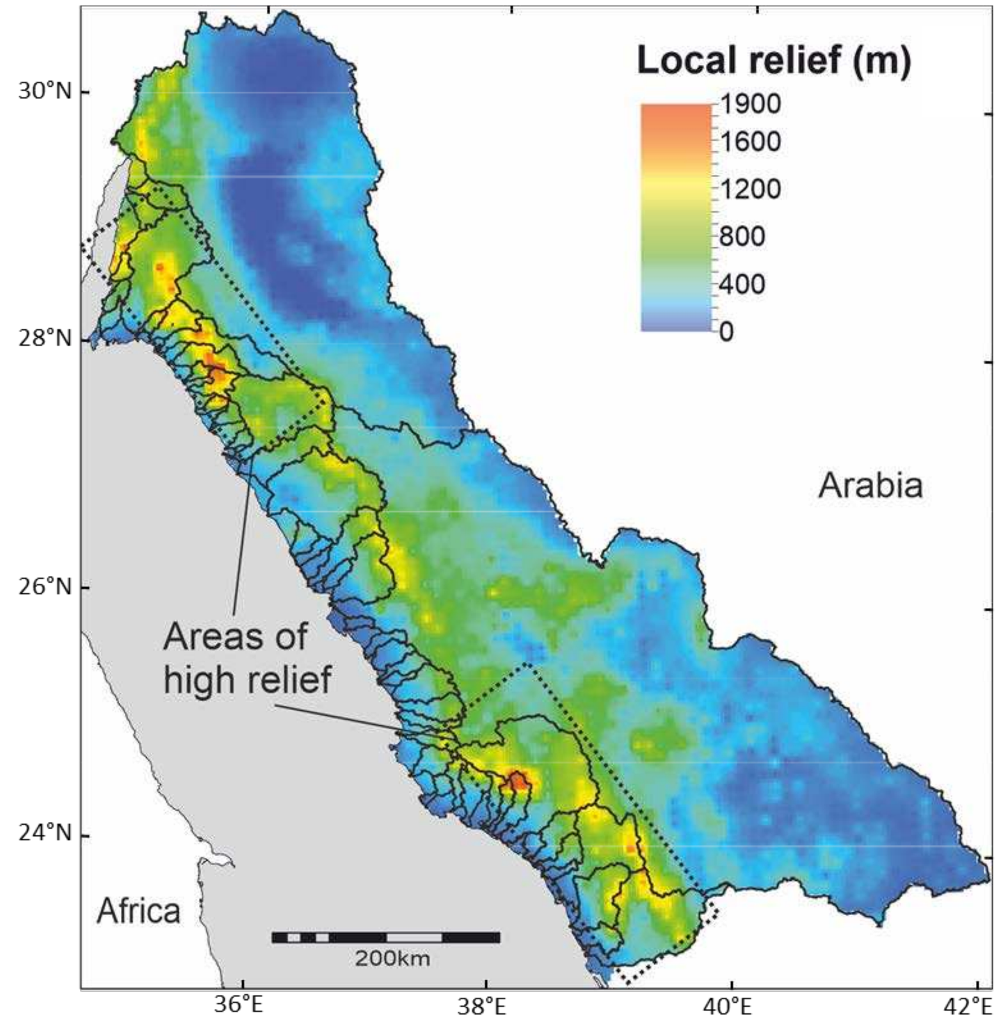

Figure 10: Local relief (10x10 km^2) map for the study area showing the areas of high relief. The catchment outlines are shown for reference.

5. Discussion

5.1. Evaluating the inverse modeling results

For the whole of Africa and Arabia, several landscape evolution simulation scenarios were run with an initial flat topography close to sea-level, each with a different climatic (precipitation rate) history as a function of space (i.e., latitude) and time by O'Malley et al. (2021) (see their Figure 13). For the study area of this work, the uplift rate histories calculated through the inversion of synthetic profiles (generated from the landscape simulations) are similar to each other and to the uplift rate history recovered by inverse modeling of observed profiles (Figure 11). Planforms are permitted to migrate but they tend not to move dramatically when advective velocity is varied via precipitation or substrate erodibility. The results indicate that changing precipitation rate makes little difference to calculated uplift histories on the length and timescales with which this paper is concerned. A similar conclusion was reached using the same approach by O'Malley et al. (2021) for Angola, the Hoggar Massif and Yemen.

Another set of landscape evolution models was run using the uplift rates recovered from the inversion of the observed profiles in this study (Figure 8) as inputs. The same erosional parameters were used as described in Section 3.1 of this work, i.e. $m = 0.2$, $v = 120\mathrm{m}^{0.6}\,\mathrm{Ma}^{-1}$. These forward models were run at a horizontal resolution of 2.5 x 2.5 km, and included both a flat initial topography and an adjusted initial topography to include a N-S gradient. These tests illuminate the effect of initial regional drainage direction (in this case, north-directed drainage) on the eventual planforms. Results show that applying an initial topographic gradient recovers some large-scale planform features (notably, the south-directed drainage in the northern part of catchment NERS20 starting from 10 Ma; Figure 12).

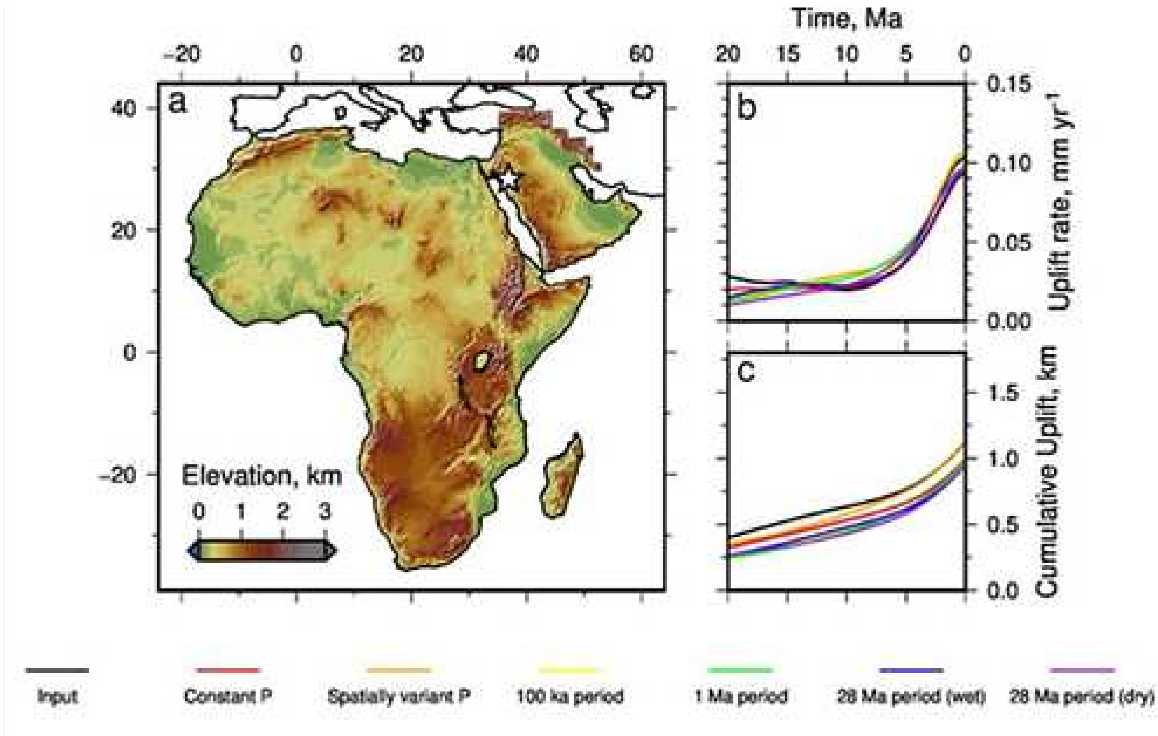

Figure 11: (a) Observed African topography. Star = locations of nodes from the inverse models of O'Malley et al. (2021) at which uplift histories are plotted. (b) Uplift rate as a function of time averaged over nine nodes at the star shown in panel (a), from O'Malley et al. (2021). Black line = uplift rate history recovered by inverse modeling of observed drainage network; colored lines = uplift rate histories recovered by inverse modeling of synthetic drainage networks generated by landscape simulations forced by original uplift rate history but subject to different precipitation histories. See guide below panels for periodicities of precipitation rate which were applied. (c) Equivalent cumulative uplift histories.

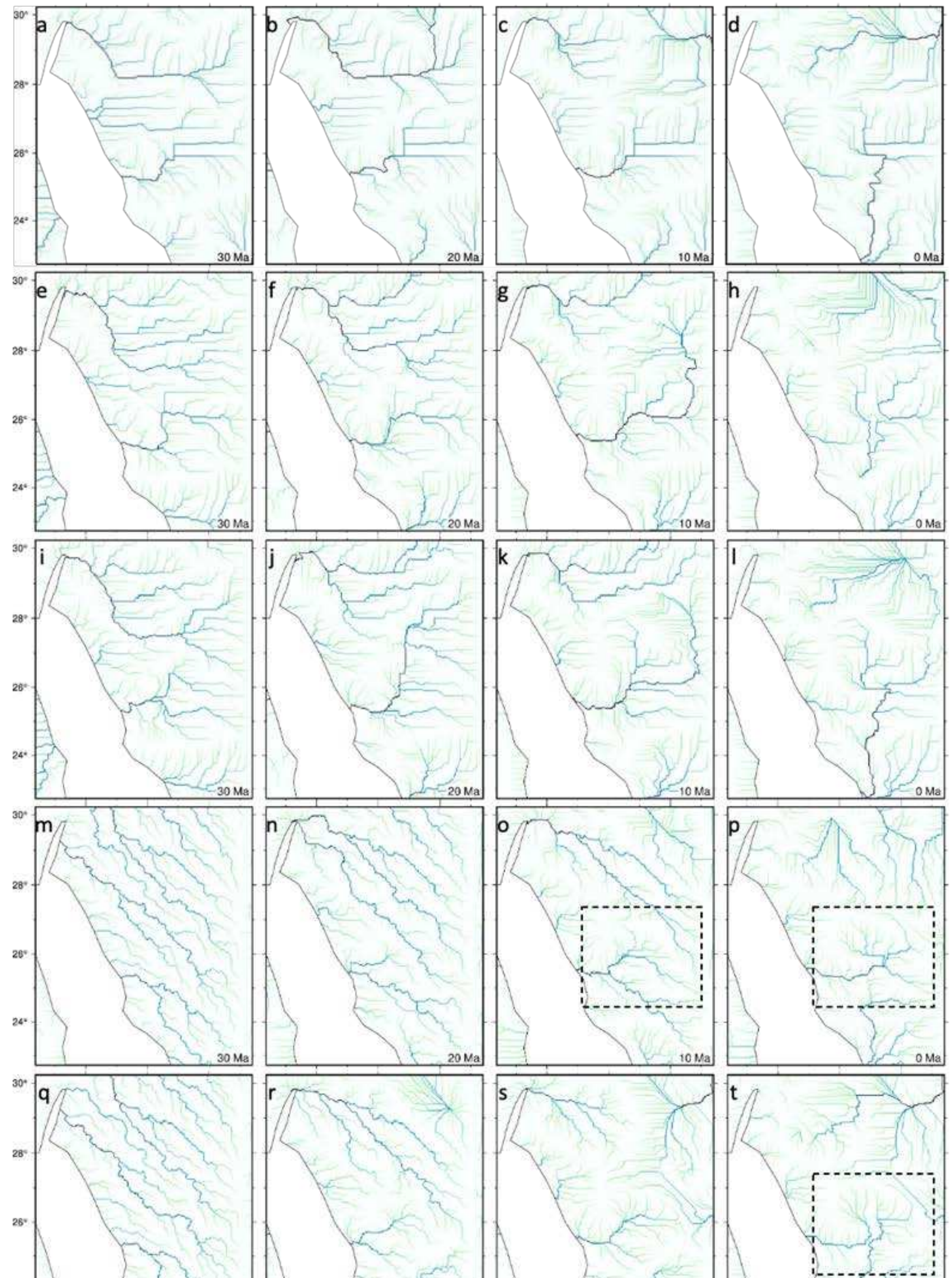

Figure 12: Output drainage planform maps from the forward landscape evolution modeling for time steps 30 Ma, 20 Ma, 10 Ma and present-day. (a-d) Assuming flat initial topography at 98 Ma. (e-h) Assuming initial topographic gradient at 98 Ma with 500 m elevation (+/- 50 m of white noise) in the south and 0 m in the north. (i-l) Same as a-d with 250 m (+/- 25 m of white noise) in the south and 0 m in the north. (m-p) Same as a-d but with the initial topographic gradient imposed at 30 Ma. (q-t) Same as e-h but with the initial topographic gradient imposed at 30 Ma. Dashed box: drainage reversal at catchment NERS20 discussed in body text.

5.2. Evolutionary model

By integrating the results of the stream profile inverse modeling and the drainage analysis, complemented with the other geomorphic descriptors (i.e., local relief and R_{va}), we propose an evolutionary model of this onshore part of Arabian margin (Figure 13). This model depicts how the drainage has been affected by pre-existing structures (that are aligned with large channels) and, more importantly, by the Cenozoic rifting and uplift.

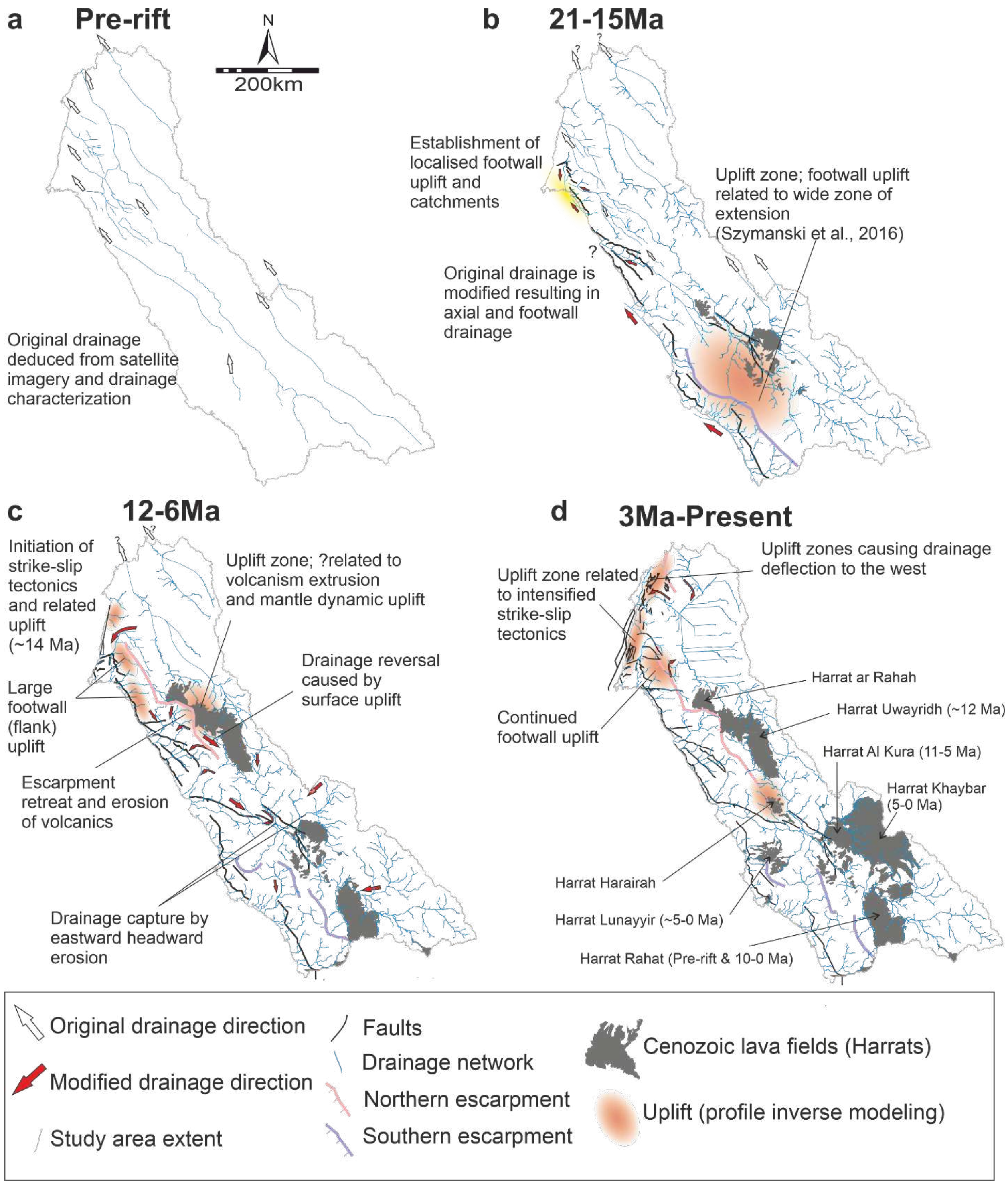

Figure 13: A multi-stage model of the NE Red Sea and eastern Gulf of Aqaba utilizing results from the inverse model and observations from the geomorphic and drainage analyses. Ages of volcanics are from Camp et al. (1991) and Bosworth et al. (2005).

5.2.1. Pre-rift drainage

The pre-rift drainage, deduced from satellite imagery and drainage characterization and complemented by highlights of paleo-drainage from the literature (e.g., Brown et al., 1989), flowed in a general northwest-ward direction (Figure 13a). The Arabian regional slope towards the north likely developed during the Oligocene in response to Afar doming (Avni et al., 2012), and may have controlled the direction of drainage in the study area. This drainage is likely to have been directed towards basins in the Levant as indicated by sediment provenance (e.g., Zilberman & Calvo, 2013).

At the catchment-scale, drainage direction would have probably been affected by NW-SE oriented heterogeneities and weaknesses in the basement (e.g., the Neoproterozoic Najd Fault System; Johnson et al., 2011). This is indicated, for instance, by the semi-linear and contiguous trends of drainage streams across NERS19, 17 and 13 catchment boundaries and the NW-oriented main channel in catchment NERS20 east of the escarpment that attest to a common NW paleo-drainage (Figure 6a-b).

Further north, at the boundary between catchments NERS1 and EGA1, the large widths of valleys hosting small streams at their uppermost reaches in the EGA1 indicate that they were located at downstream areas of a paleo-drainage system (Figures 6a and 6d). Although this interpretation suggests dominantly west-ward direction for these valleys, they are interpreted here to be distributaries of a large paleo-drainage system. Being in this northern part of the study area and in the larger context discussed earlier, these mounting observations support an overall north-directed paleo-drainage interpretation.

5.2.2. Early to main rift-related uplift (21-15 Ma)

Denudation does not necessarily equate to uplift but it is probably reasonable to assume that relative base-level drop driven by rock uplift can result in denduation. Early Miocene uplift in the southern part of the study area estimated from the inverse modeling (Figure 8b) falls within published tectonic denudation age estimates that signify normal faulting (Bosworth, 2015 and references therein). High R_{va} (catchments NERS37 and 42) and local relief values in this area are likely caused by the relative high values of uplift rate and subsequent erosion (Figures 9 and 10). As relief and R_{va} are measurements of the present-day topography, they cannot be linked directly to temporal changes in uplift rate. However, the positive correlation between relief/R_{va} and cumulative uplift supports the modeled distribution of uplift in space.

Furthermore, the end of the diffuse extension phase and migration of faulting towards the Red Sea basin at ~13 Ma proposed by Szymanski et al. (2016) at the Central Arabian Rift Flank (CARF) is reflected in the drainage inverse model whereby the uplift zone narrows down from 21 Ma to 15 Ma before disappearing at 12 Ma (Figure 8b). The Early Miocene uplift is also supported by the existence of early rift granitic conglomerates in early rift basins, which indicate crestal erosion of the uplifted basement (Figure 3c; Hughes et al., 1999).

Uplift in the northern part of the study area is not resolved until 15 Ma (Figure 8b), implying that resolvable uplift commenced between 18 and 15 Ma. This might indicate that the initial fault segments did not coalesce until the early Middle Miocene as supported, for example, by the structural context of a Late Burdigalian carbonate platform interpreted in Koeshidayatullah et al. (2016) to have developed within a relay zone that later became breached by a through-going basin-bounding fault. Geomorphic indications of uplift are grasped from the oblique Gulf of Aqaba catchments (e.g., EGA21 and 23) that are more perpendicular to the Red Sea axis, suggesting inheritance of incision of early uplifted footwall (i.e., prior to transform tectonics).

During this and the next tectonic stage, drainage had likely reorganized to form rift-related catchments that are affected by the positions of rift basins and their bounding faults (Figure 13b). For instance, catchments with areas <1000 km^2 that are located to the north and south of NERS1 outlet represent footwall drainage given their sizes and positions with respect to the bounding faults (e.g., NERS6-8 and NERS22-36; Figure 3b). Larger catchments (1000-7000 km^2) are likely to have formed as catchments behind the original footwall watershed (e.g., NERS13) or at early rift relay zones (e.g., NERS1, 4, 11 and 37) as indicated by their positions with respect to faults (Figure 3).

The shape of the largest drainage catchment (NERS20) suggests an earlier NW-SE-elongated pre-rift catchment that deviates from the typical rift-related drainage (see previous sub-section). Miocene rifting resulted in the incorporation of this drainage first as an axial drainage in early inboard rift basins (Szymanski et al., 2016) before being captured by eastward fluvial erosion during the Middle Miocene.

5.2.3. Oblique extension and early strike-slip tectonics: northward shift of uplift (15-6 Ma)

The onset of the strike-slip tectonics along the Gulf of Aqaba was associated with oblique extension and localized deformation both along the gulf and in the northern Red Sea (~14-12 Ma; Bosworth et al., 2005; Koeshidayatullah et al., 2016; Tubbs et al., 2014). The northward shift of the uplift locus during and after this period (Figure 8b) was likely due to coalescence of fault segments (e.g., that resulted in relay ramp breaching; Koeshidayatullah et al.,2016), and the initiation of the strike-slip tectonics. The relatively short wavelengths and high uplift rates (~60 km and 0.14 mm/a, respectively) support the conclusion of uplift due to normal faulting.

Pre-existing fault scarps continued to retreat as, for instance, erosion continued of the Harrat Uwayridh/ar Rahah ~12 Ma-volcanics (Bosworth et al., 2005; Figure 13c). This age falls within the estimated uplift timing to the northwest (12-9 Ma) suggesting a potential driver for enhanced erosion (Figure 8b). Geochemically, the volcanics were interpreted to be derived from direct mantle melting (Camp & Roobol, 1992), suggesting mantle upwelling as a force for uplift. This agrees with the conclusion of Ball et al. (2021) who, using global Neogene-Quaternary volcanic rock geochemical data and shear wave velocities, demonstrate that intraplate uplifted volcanic rocks are primarily underlain by high-temperature upper mantle.

It is important to note that misfit between observed and modeled stream profiles at the northern part of the northern Red Sea margin, where uplift is predicted during the time period from 12- 6 Ma, is the largest compared to the other parts of the margin (Figure 7e-f). We interpret this to reflect the role played by factors other than uplift (e.g., lithological variation affecting rock strength) in shaping the stream profiles. However, this does not rule out the role played by the uplift completely where, for example, convex drainage profiles are all within predominantly granitic rocks on the Gulf of Aqaba margin (Figures 3c and 7a).

5.2.4. Intensification of strike-slip tectonics (3-0 Ma)

Strike-slip tectonics and the strain localization along the northern area faults were associated with even higher uplift rates (Figures 8b and 13d). Along the Gulf of Aqaba margin, profile convexities (Figure 7a) signify a transient state with ongoing net uplift, whereby uplift rate exceeds erosion rate (Whittaker, 2012). Estimated uplift rates from the inverse model (mean uplift rate $\approx$ 0.17 mm/a; cumulative uplift $\approx$ 1.66 km; 15-0 Ma; Figure 8b) are in close agreement with estimates from elevated Pleistocene coral terraces along the eastern side of the Gulf (0.15 mm/a between125-0 ka) and conceptual projection of basement top assuming a near sea-level paleo-topography (0.12-0.16 mm/a between 14-11 Ma; Bosworth et al., 2017). Bosworth et al. (2017) concluded that a significant dip component accompanies the strike-slip tectonics. This agrees with the Gulf of Aqaba being largely a set of pull-apart basins with normal bounding faults separating the basins from uplifted areas on the flank.

Geomophologically, misfit streams along the eastern boundary of NERS1 were likely related to drainage reversal during this or the previous uplift phase (Figures 5 and 10c-d). Furthermore, the high relief and R_{va} value for NERS1 compared to EGA1 suggest incision by NERS1 headwaters into the low relief landscape of EGA1 (Figure 9), pushing the boundary between the two catchments towards the east. Therefore, the effect of the uplift was to introduce 1) an axis of uplift where drainage is reversed towards the east then to the north in EGA1 and 2) incision in the east-ward headwaters of NERS1 resulting in drainage area gain at the expense of EGA1 and generating the relief contrast between the two catchments.

5.3. Geodynamic implications: on the contribution of mantle support

Plate-scale uplift of the Arabian margin has been suggested to be caused by a long-wavelength plate tilt driven by mantle flow upwelling (Japsen et al., 2012); a young uplift (~12 Ma; Daradich et al., 2003) compared with the early rift-related uplift. This mantle support is also indicated by relatively thin lithosphere beneath the elevated flank (<70 km; Hansen et al., 2007) and low mantle shear velocity (Hansen et al., 2008; Park et al., 2008; Yao et al., 2017), and revealed using uplift estimation through inversion of river profiles (Wilson et al., 2014).

The estimated uplift in the southern part of the study area lies north of a dynamically supported regional uplift zone in southwestern Arabia interpreted by Wilson et al. (2014). The timing of the uplift across the southern part of the study area vis-à-vis rifting is similar to that of the rift-related exhumation concluded by Szymanski et al. (2016) for the Central Arabian Rift Flank due to mechanical unloading by normal faulting. Additionally, the long uplift wavelength (~200 km; 21-15 Ma times in Figure 8b) suggests a possible additional dynamic uplift possibly due to mantle upwelling during the early rift phase. This latter conclusion is made here with caution given that the model coverage deteriorates back in time.

A relatively low-velocity zone exists in the mantle (65-85 km depth) beneath in the southern part of our study area and continues northward to just southwest of Harrat Uwayridh/ar Rahah (Yao et al., 2017). This zone coincides with an uplift zone with a rate that has been increasing from 3 Ma to the present (Figure 8b). The spatial coincidence of this low-velocity zone in the mantle, the existence of young volcanics (<12 Ma) and the increasing uplift rate all indicate dynamic support by mantle material beneath the rift flank at least after the Middle Miocene.

Elsewhere in the study area, the short period, if any, separating rifting from the uplift compared with mature passive margins (discussed in Japsen et al., 2012) indicate that the bulk of the uplift is related to rifting processes and later transform tectonics. The uplift in the northernmost part of the study area is underlain by higher-than-average shear wave velocities (e.g., Yao et al., 2017) reducing the possibility of an asthenospheric dynamic support. The lack of volcanism in this part of the margin and the relatively large amount of cumulative uplift (Figure 8a) support such a conclusion.

6. Conclusions

A workflow integrating drainage network analysis and inverse modeling to estimate Cenozoic uplift is implemented to investigate the onshore evolution of NE Red Sea and the nearby eastern Gulf of Aqaba margins. The workflow benefits from its dependency on ubiquitous drainage data and geomorphic metrics. Such ubiquity makes the workflow application to other geologic settings feasible. In this study area, the catchments and streams reflect the interplay of basement heterogeneities, the tectonic (i.e., rifting and transform tectonics) and geomorphic evolution. Along-margin spatial geomorphic variation (minimum erosion and local relief) is interpreted to be associated with south-to-north spatio-temporal variation in uplift rate and magnitude. The uplift history records early uplift in the southern part of the study area and a later uplift in the north. Integrating our results with other geological observations (e.g. volcanism) indicates that early-rift uplift might have been caused by unloading due to normal faulting with possible additional mantle dynamic support. We tentatively suggest that later uplift was driven by fault coalescence, strain partitioning near transform tectonics and asthenospheric upwelling.

Acknowledgments and Data

- ASTER GDEM is a product of NASA and METI and can be downloaded from https://gdex.cr.usgs.gov/gdex/.
- Input data for inverse modeling: https://doi.org/10.6084/m9.figshare.19519096.v1; output uplift rates: https://doi.org/10.6084/m9.figshare.19514332.v1; output cumulative uplift: https://doi.org/10.6084/m9.figshare.19514326.v1
- We thank Dr. Estelle Mortimer for providing constructive feedback.

References

Avni, Y., Segev, A. & Ginat, H. (2012). Oligocene regional denudation of the northern Afar dome: Pre- and syn-breakup stages of the Afro-Arabian plate. *Geological Society of America Bulletin, 124* (11-12), 1871-1897. https://doi.org/10.1130/B30634.1

Ball, P. W., White, N. J., Maclennan, J., & Stephenson, S. N. (2021). Global influence of mantle temperature and plate thickness on intraplate volcanism. *Nature communications*, *12*(1), 1-13. https://doi.org/10.1038/s41467-021-22323-9

Bellin, N., Vanacker, V. & Kubik, P.W. (2014). Denudation rates and tectonic geomorphology of the Spanish Betic Cordillera. *Earth and Planetary Science Letters, 390*, 19-30. https://doi.org/10.1016/j.epsl.2013.12.045

Bohannon, R. G., Naeser, C. W., Schmidt, D. L., & Zimmermann, R. A. (1989). The timing of uplift, volcanism, and rifting peripheral to the Red Sea: a case for passive rifting?. *Journal of Geophysical Research: Solid Earth*, *94*(B2), 1683-1701. https://doi.org/10.1029/JB094iB02p01683

Bosworth, W. (2015). Geological evolution of the Red Sea: historical background, review, and synthesis. In N. M. A. Rasul, I.C.F. Stewart (Eds.), *The Red Sea: The Formation, Morphology, Oceanography and Environment of a Young Ocean Basin* (pp. 45-78). Berlin, Heidelberg, Springer. https://doi.org/10.1007/978-3-662-45201-1_3

Bosworth, W., & McClay, K. (2001). Structural and stratigraphic evolution of the Gulf of Suez rift, Egypt: a synthesis. *Mémoires du Muséum national d'histoire naturelle*, *186*, 567-606.

Bosworth, W., Huchon, P., & McClay, K. (2005). The red sea and gulf of aden basins. *Journal of African Earth Sciences*, *43*(1-3), 334-378. https://doi.org/10.1016/j.jafrearsci.2005.07.020

Bosworth, W., Crevello, P., Winn, R. D., & Steinmetz, J. (1998). Structure, sedimentation, and basin dynamics during rifting of the Gulf of Suez and north-western Red Sea. In B. H. Purser, D.W. Bosence (Eds.), *Sedimentation and Tectonics in Rift Basins Red Sea:-Gulf of Aden* (pp. 77-96). Dordrecht, Springer. https://doi.org/10.1007/978-94-011-4930-3_6

Bosworth, W., Montagna, P., Pons-Branchu, E., Rasul, N., & Taviani, M. (2017). Seismic hazards implications of uplifted Pleistocene coral terraces in the Gulf of Aqaba. *Scientific Reports*, *7*(1), 1-13. https://doi.org/10.1038/s41598-017-00074-2

Brown, G. F., Schmidt, D. L., & Huffman Jr, A. C. (1989). *Geology of the Arabian Peninsula; shield area of western Saudi Arabia* (No. 560-A). US Geological Survey.

Burke, K. & Gunnell, Y. (2008). The African erosion surface: a continental-scale synthesis of geomorphology, tectonics, and environmental change over the past 180 million years. *Geological Society of America Memoir, 201*, 1-66.

Bursztyn, N., Pederson, J. L., Tressler, C., Mackley, R. D. & Mitchell, K. J. (2015). Rock strength along a fluvial transect of the Colorado Plateau–quantifying a fundamental control on geomorphology. *Earth and Planetary Science Letters, 429*, 90-100.

Camp, V. E., Roobol, M. J., & Hooper, P. R. (1991). The Arabian continental alkali basalt province: Part II. Evolution of Harrats Khaybar, Ithnayn, and Kura, Kingdom of Saudi Arabia. *Geological Society of America Bulletin*, *103*(3), 363-391. https://doi.org/10.1130/0016-7606(1991)103<0363:TACABP>2.3.CO;2

Camp, V. E., & Roobol, M. J. (1992). Upwelling asthenosphere beneath western Arabia and its regional implications. *Journal of Geophysical Research: Solid Earth, 97*(B11), 15255-15271. https://doi.org/10.1029/92JB00943

Cochran, J. R. (2005). Northern Red Sea: Nucleation of an oceanic spreading center within a continental rift. *Geochemistry, Geophysics, Geosystems*, *6*(3). https://doi.org/10.1029/2004GC000826

Coleman, R. G., Gregory, R. T., & Brown, G. F. (1983). *Cenozoic volcanic rocks of Saudi Arabia* (No. 83-788). US Geological Survey. https://doi.org/10.3133/ofr83788

Daradich, A., Mitrovica, J. X., Pysklywec, R. N., Willett, S. D., & Forte, A. M. (2003). Mantle flow, dynamic topography, and rift-flank uplift of Arabia. *Geology*, *31*(10), 901-904. https://doi.org/10.1130/G19661.1

Doglioni, C., Carminati, E., & Bonatti, E. (2003). Rift asymmetry and continental uplift. *Tectonics*, *22*(3). https://doi.org/10.1029/2002TC001459

Forte, A. M. & Whipple, K.X. (2018). Criteria and tools for determining drainage divide stability. *Earth and Planetary Science Letters, 493*, 102-117. https://doi.org/10.1016/j.epsl.2018.04.026

Gallen, S. F. (2018). Lithologic controls on landscape dynamics and aquatic species evolution in post-orogenic mountains. *Earth and Planetary Science Letters, 493*, 150-160. https://doi.org/10.1016/j.epsl.2018.04.029

Gawthorpe, R. L., Sharp, I., Underhill, J. R., & Gupta, S. (1997). Linked sequence stratigraphic and structural evolution of propagating normal faults. *Geology*, *25*(9), 795-798. https://doi.org/10.1130/0091-7613(1997)025%3C0795:LSSASE%3E2.3.CO;2

Giaconia, F., Booth-Rea, G., Martínez-Martínez, J.M., Azañón, J.M., Pérez-Peña, J.V., Pérez-Romero, J. & Villegas, I. (2012). Geomorphic evidence of active tectonics in the Sierra Alhamilla (eastern Betics, SE Spain). *Geomorphology, 145*, 90-106. https://doi.org/10.1016/j.geomorph.2011.12.043

Gilchrist, A.R. & Summerfield, M.A. (1990). Differential denudation and flexural isostasy in formation of rifted-margin upwarps. *Nature, 346*(6286), 739-742. https://doi.org/10.1038/346739a0

Goren, L., Fox, M. & Willett, S. D. (2014). Tectonics from fluvial topography using formal linear inversion: Theory and applications to the Inyo Mountains, California. *Journal of Geophysical Research: Earth Surface, 119*(8), 1651-1681. https://doi.org/10.1002/2014JF003079

Griffin, D. L. (1999). The late Miocene climate of northeastern Africa: unravelling the signals in the sedimentary succession. *Journal of the Geological Society*, *156*(4), 817-826. https://doi.org/10.1144/gsjgs.156.4.0817

Hansen, S. E., Gaherty, J. B., Schwartz, S. Y., Rodgers, A. J., & Al-Amri, A. (2008). Seismic velocity structure and depth-dependence of anisotropy in the Red Sea and Arabian shield from surface wave analysis. *Journal of Geophysical Research: Solid Earth, 113*(B10). https://doi.org/10.1029/2007JB005335

Hansen, S. E., Rodgers, A. J., Schwartz, S. Y., & Al-Amri, A. M. (2007). Imaging ruptured lithosphere beneath the Red Sea and Arabian Peninsula. *Earth and Planetary Science Letters*, *259*(3-4), 256-265. https://doi.org/10.1016/j.epsl.2007.04.035

Haq, B.U. & Al-Qahtani, A.M. (2005). Phanerozoic cycles of sea-level change on the Arabian Platform. *GeoArabia, 10*(2), 127-160.

Hobley, D. E., Adams, J. M., Siddhartha Nudurupati, S., Hutton, E. W., Gasparini, N. M., Istanbulluoglu, E., & Tucker, G. E. (2017). Creative computing with Landlab: An open-source toolkit for building, coupling, and exploring two-dimensional numerical models of Earth-surface dynamics. *Earth Surface Dynamics, 5*(1), 21-46. https://doi.org/10.5194/esurf-5-21-2017

Hughes, G. W., & Filatoff, J. (1995). New biostratigraphic constraints on Saudi Arabian Red Sea pre-and syn-rift sequences. *Middle East petroleum geosciences*, *94*, 517-528.

Hughes, G. W., Perincek, D., Grainger, D. J., Abu-Bshait, A. J., & Jarad, A. R. M. (1999). Lithostratigraphy and depositional history of part of the Midyan region, northwestern Saudi Arabia. *GeoArabia*, *4*(4), 500-542.

Ilani, S., Harlavan, Y., Tarawneh, K., Rabba, I., Weinberger, R., Ibrahim, K., et al. (2001). New K-Ar ages of basalts from the Harrat Ash Shaam volcanic field in Jordan: Implications for the span and duration of the upper-mantle upwelling beneath the western Arabian plate. *Geology*, *29*(2), 171-174. https://doi.org/10.1130/0091-7613(2001)029%3C0171:NKAAOB%3E2.0.CO;2

Japsen, P., Chalmers, J. A., Green, P. F., & Bonow, J. M. (2012). Elevated, passive continental margins: Not rift shoulders, but expressions of episodic, post-rift burial and exhumation. *Global and Planetary Change*, *90*, 73-86. https://doi.org/10.1016/j.gloplacha.2011.05.004

Johnson, P. R., Andresen, A., Collins, A. S., Fowler, A. R., Fritz, H., Ghebreab, W., Kusky, T. & Stern, R. J. (2011). Late Cryogenian–Ediacaran history of the Arabian–Nubian Shield: a review of depositional, plutonic, structural, and tectonic events in the closing stages of the northern East African Orogen. *Journal of African Earth Sciences, 61*(3), 167-232. https://doi.org/10.1016/j.jafrearsci.2011.07.003

Kirby, E. & Whipple, K.X. (2012). Expression of active tectonics in erosional landscapes. *Journal of Structural Geology, 44*, 54-75. https://doi.org/10.1016/j.jsg.2012.07.009

Koeshidayatullah, A., Al-Ramadan, K., Collier, R. & Hughes, G. W. (2016). Variations in architecture and cyclicity in fault-bounded carbonate platforms: Early Miocene Red Sea Rift, NW Saudi Arabia. *Marine and Petroleum Geology, 70*, 77-92. https://doi.org/10.1016/j.marpetgeo.2015.10.017

Kohn, B. P. & Eyal, M. (1981). History of uplift of the crystalline basement of Sinai and its relation to opening of the Red Sea as revealed by fission track dating of apatites. *Earth and Planetary Science Letters, 52*, 129-141. https://doi.org/10.1016/0012-821X(81)90215-6

O'Callaghan, J. F., & Mark, D. M. (1984). The extraction of drainage networks from digital elevation data. *Computer vision, graphics, and image processing*, *28*(3), 323-344. https://doi.org/10.1016/S0734-189X(84)80011-0

O'Malley, C., White, N., Stephenson, S., & Roberts, G. (2021). Large-Scale Tectonic Forcing of the African Landscape. *Journal of Geophysical Research: Earth Surface, 126*(12). https://doi.org/10.1029/2021JF006345

Omar, G. I., Steckler, M. S., Buck, W. R., & Kohn, B. P. (1989). Fission-track analysis of basement apatites at the western margin of the Gulf of Suez rift, Egypt: evidence for synchroneity of uplift and subsidence. *Earth and Planetary Science Letters*, *94*(3-4), 316-328. https://doi.org/10.1016/0012-821X(89)90149-0

Osmundsen, P. T., & Redfield, T. F. (2011). Crustal taper and topography at passive continental margins. *Terra Nova, 23*(6), 349-361. https://doi.org/10.1111/j.1365-3121.2011.01014.x

Pallister, J. S. (1987). Magmatic history of Red Sea rifting: Perspective from the central Saudi Arabian coastal plain. *Geological Society of America Bulletin*, *98*(4), 400-417.

Park, Y., Nyblade, A. A., Rodgers, A. J. & Al-Amri, A. (2008). S wave velocity structure of the Arabian Shield upper mantle from Rayleigh wave tomography. *Geochemistry, Geophysics, Geosystems, 9*(7). https://doi.org/10.1029/2007GC001895

Paul, J. D., Roberts, G. G., & White, N. (2014). The African landscape through space and time. *Tectonics, 33*(6), 898-935. https://doi.org/10.1002/2013TC003479

Perron, J. T. & Royden, L. (2013). An integral approach to bedrock river profile analysis. *Earth Surface Processes and Landforms, 38*(6), 570-576. https://doi.org/10.1002/esp.3302

Plaziat, J. C., Baltzer, F., Choukri, A., Conchon, O., Freytet, P., Orszag-Sperber, F., et al. (1998). Quaternary marine and continental sedimentation in the northern Red Sea and Gulf of Suez (Egyptian coast): influences of rift tectonics, climatic changes and sea-level fluctuations. In *Sedimentation and Tectonics in Rift Basins Red Sea-Gulf of Aden* (pp. 537-573). Springer, Dordrecht. https://doi.org/10.1007/978-94-011-4930-3_29

Powell, J. H., Abed, A. M., and Nindre, L. (2014). Cambrian stratigraphy of Jordan. *GeoArabia-Middle East Petroleum Geosciences. 19*(3), 81-134.

Pritchard, D., Roberts, G. G., White, N. J., & Richardson, C. N. (2009). Uplift histories from river profiles. *Geophysical Research Letters*, *36*(24). https://doi.org/10.1029/2009GL040928

Roberts, G. G., & White, N. (2010). Estimating uplift rate histories from river profiles using African examples. *Journal of Geophysical Research: Solid Earth*, *115*(B2). https://doi.org/10.1029/2009JB006692

Roberts, G. G., Paul, J. D., White, N. & Winterbourne, J. (2012). Temporal and spatial evolution of dynamic support from river profiles: A framework for Madagascar. *Geochemistry, Geophysics, Geosystems, 13*(4). https://doi.org/10.1029/2012GC004040

Roberts, G. G., White, N., & Lodhia, B. H. (2019). The generation and scaling of longitudinal river profiles. *Journal of Geophysical Research: Earth Surface, 124*(1), 137-153. https://doi.org/10.1029/2018JF004796

Rosenbloom, N. A., & Anderson, R. S. (1994). Hillslope and channel evolution in a marine landscape, Santa Cruz, California. *Journal of Geophysical Research, 99*(B7), 14,013–14,029. https://doi.org/10.1029/94JB00048

Rudge, J. F., Roberts, G. G., White, N. J., & Richardson, C. N. (2015). Uplift histories of Africa and Australia from linear inverse modeling of drainage inventories. *Journal of Geophysical Research: Earth Surface, 120*, 894–914. https://doi.org/10.1002/2014JF003297

Salles, T., & Hardiman, L. (2016). Badlands: An open-source, flexible and parallel framework to study landscape dynamics. *Computers & Geosciences, 91*, 77-89. https://doi.org/10.1016/j.cageo.2016.03.011

Saudi Geologial Survey. Surface Geology Maps of the Arabian Peninsula, Scale: 250 000, Saudi Geological Survey, 1977-2016

Snyder, N. P., Whipple, K. X., Tucker, G. E. and Merritts, D. J. (2000). Landscape response to tectonic forcing: Digital elevation model analysis of stream profiles in the Mendocino triple junction region, northern California. *Geological Society of America Bulletin, 112*(8), 1250-1263. https://doi.org/10.1130/0016-7606(2000)112

Steckler, M. S., Berthelot, F., Lyberis, N., & Le Pichon, X. (1988). Subsidence in the Gulf of Suez: implications for rifting and plate kinematics. *Tectonophysics, 153*(1-4), 249-270. https://doi.org/10.1016/0040-1951(88)90019-4

Strahler, A. N. (1957). Quantitative analysis of watershed geomorphology. Eos, Transactions American *Geophysical Union*, *38*(6), 913-920. https://doi.org/10.1029/TR038i006p00913

Szymanski, E., Stockli, D. F., Johnson, P. R., & Hager, C. (2016). Thermochronometric evidence for diffuse extension and two-phase rifting within the Central Arabian Margin of the Red Sea Rift. *Tectonics*, *35*(12), 2863-2895. https://doi.org/10.1002/2016TC004336

Tarboton, D. G., Bras, R. L., & Rodriguez-Iturbe, I. (1991). On the extraction of channel networks from digital elevation data. *Hydrological processes*, *5*(1), 81-100. https://doi.org/10.1002/hyp.3360050107

Tubbs, R. E., Fouda, H., Afifi, A., Raterman, N., Hughes, G., & Fadolalkarem, Y. (2014). Midyan Peninsula, northern Red Sea, Saudi Arabia: seismic imaging and regional interpretation. *GeoArabia*, *19*(3), 165-184.

Twidale, C. R. (2004). River patterns and their meaning. *Earth-Science Reviews*, *67*(3-4), 159-218. https://doi.org/10.1016/j.earscirev.2004.03.001

Walford, H. L., & White, N. J. (2005). Constraining uplift and denudation of west African continental margin by inversion of stacking velocity data. *Journal of Geophysical Research: Solid Earth, 110*(B4). https://doi.org/10.1029/2003JB002893

Wapenhans, I., Fernandes, V. M., O'Malley, C., White, N., Roberts, G. G., & Watts, A. B. (2021). Scale-dependent contributors to river profile geometry. *Journal of Geophysical Research: Earth Surface, 126*, 909-914. https://doi.org/10.1029/2020jf005879

Weissel, J. K., & Karner, G. D. (1989). Flexural uplift of rift flanks due to mechanical unloading of the lithosphere during extension. *Journal of Geophysical Research: Solid Earth, 94*(B10), 13919-13950.

Whipple, K.X., Forte, A.M., DiBiase, R.A., Gasparini, N.M. & Ouimet, W.B. (2017). Timescales of landscape response to divide migration and drainage capture: Implications for the role of divide mobility in landscape evolution. *Journal of Geophysical Research: Earth Surface, 122*(1), 248-273. https://doi.org/10.1002/2016JF003973

Whipple, K. X. & Tucker, G. E. (1999). Dynamics of the stream-power river incision model: Implications for height limits of mountain ranges, landscape response timescales, and research needs. *Journal of Geophysical Research: Solid Earth, 104*(B8), 17661-17674. https://doi.org/10.1029/1999JB900120

Whittaker, A.C. (2012). How do landscapes record tectonics and climate?. *Lithosphere, 4*(2), 160-164. https://doi.org/10.1130/RF.L003.1

Willett, S.D., McCoy, S.W., Perron, J.T., Goren, L. & Chen, C.Y. (2014). Dynamic reorganization of river basins. *Science, 343*(6175). https://doi.org/10.1126/science.1248765

Wilson, J. W. P., Roberts, G. G., Hoggard, M. J., & White, N. J. (2014). Cenozoic epeirogeny of the Arabian Peninsula from drainage modeling. *Geochemistry, Geophysics, Geosystems*, *15*(10), 3723-3761. https://doi.org/10.1002/2014GC005283

Wobus, C.W., Tucker, G.E. & Anderson, R.S. (2010). Does climate change create distinctive patterns of landscape incision?. *Journal of Geophysical Research: Earth Surface, 115*(F4). https://doi.org/10.1029/2009JF001562

Yao, Z., Mooney, W. D., Zahran, H. M., & Youssef, S. E. H. (2017). Upper mantle velocity structure beneath the Arabian shield from Rayleigh surface wave tomography and its implications. *Journal of Geophysical Research: Solid Earth, 122*(8), 6552-6568. https://doi.org/10.1002/2016JB013805

Zilberman, E., & Calvo, R. (2013). Remnants of Miocene fluvial sediments in the Negev Desert, Israel, and the Jordanian Plateau: Evidence for an extensive subsiding basin in the northwestern margins of the Arabian plate. *Journal of African Earth Sciences, 82*, 33-53. https://doi.org/10.1016/j.jafrearsci.2013.02.006